This article appeared in

Liu, G., Wong, W. S. Y., Kraft, M., Ager, J. W., Vollmer, D., & Xu, R. (2021). Wetting-regulated gas-involving (photo)electrocatalysis: biomimetics in energy conversion. *Chemical Society Reviews, 50*(18), 10674-10699. doi:10.1039/d1cs00258a.

DOI: 10.1039/d1cs00258a

Wetting-regulated gas-involving (photo)electrocatalysis: biomimetics in energy conversion

Guanyu Liu, William S. Y. Wong, Markus Kraft, Joel W. Ager, Doris Vollmer, Rong Xu*

Chem. Soc. Rev., 2021,50, 10674-10699, https://doi.org/10.1039/D1CS00258A

Wetting-Regulated Gas-Involving (Photo)electrocatalysis: Biomimetics in Energy Conversion

Guanyu Liu,[ab] *William S. Y. Wong,*[c] *Markus Kraft,*[bd] *Joel W. Ager,*[ef] *Doris Vollmer,*[c] *Rong Xu*[*ab]

[a]School of Chemical & Biomedical Engineering, Nanyang Technological University, 62 Nanyang Drive, 637459 Singapore

[b]Cambridge Centre for Advanced Research and Education in Singapore (CARES), CREATE Tower, 1 Create Way, 138602 Singapore

[c]Max Planck Institute for Polymer Research, Ackermannweg 10, D-55128, Mainz, Germany

[d]Department of Chemical Engineering and Biotechnology, University of Cambridge, West Cambridge Site, Philippa Fawcett Drive, Cambridge CB3 0AS, United Kingdom

[e]Department of Materials Science and Engineering, University of California, Berkeley, California 94720, United States

[f]Berkeley Educational Alliance for Research in Singapore (BEARS), CREATE Tower, 1 Create Way, 138602 Singapore

*To whom correspondence should be addressed: R.X. (email: rxu@ntu.edu.sg)

Chem. Soc. Rev., 2021,50, 10674-10699, https://doi.org/10.1039/D1CS00258A

ABSTRACT

(Photo)electrolysis of water or gases with water to species serving as industrial feedstocks and energy carriers, such as hydrogen, ammonia, ethylene, propanol, *etc.*, has drawn tremendous attention. Moreover, these processes can often be driven by renewable energy under ambient conditions as a sustainable alternative to traditional high-temperature and high-pressure synthesis methods. In addition to the extensive studies on catalyst development, increasing attention has been paid to regulation of gas transport/diffusion behaviors during gas-involving (photo)electrocatalytic reactions towards the goal of creating industrially viable catalytic systems with high reaction rates, excellent long-term stability and near-unity selectivity. Biomimetic surfaces and systems with special wetting capabilities and structural advantages can shed light on the future design of (photo)electrodes and address long-standing challenges. This article is dedicated to bridging the fields of wetting and catalysis by reviewing cutting-edge design methodologies of both gas-evolving and gas-consuming (photo)electrocatalytic systems. We first introduce the fundamentals of various in-air/underwater wetting states and their corresponding bioinspired structural properties. The relationship amongst bubble transport behaviors, wettability, and porosity/tortuosity are also discussed. Next, the latest implementations of wetting-related design principles for gas-evolving reactions (*i.e.* hydrogen evolution reaction and oxygen evolution reaction) and gas-consuming reactions (*i.e.* oxygen reduction reaction and CO_2 reduction reaction) are summarized. For photoelectrode designs, additional factors are taken into account, such as light absorption and the separation, transport and recombination of photoinduced electrons and holes. The influences of wettability and 3D structuring of (photo)electrodes on the catalytic activity, stability and selectivity are analyzed to reveal the underlying mechanisms. Finally, remaining questions and related future perspectives are outlined.

Chem. Soc. Rev., 2021,50, 10674-10699, https://doi.org/10.1039/D1CS00258A

1. Introduction

Maximizing energy harvest and storage from sunlight striking our planet's surface can sustainably meet the increasing energy demand while reducing the carbon footprint. Photovoltaic cells have been commercially available to convert solar energy into electrical energy.[1] However, there remain a number of issues including the intermittent availability of solar energy and waste of excessive amount of electrical energy, which could be addressed via large-scale energy storage in the form of chemical bonds, such as H_2 with high energy density of 122 kJ g^{-1}.[2] Later on the electrical energy can be efficiently regenerated using fuel cells. High-value-added chemicals such as ammonia, ethylene and propanol as industrial feedstocks can also be produced by consuming solar/electrical energy, water and atmospheric gases.

(Photo)electrocatalysis plays a crucial role in the aforementioned energy conversion and storage processes towards a sustainable future. Based on the roles of gases as products or reactants, gas-involving (photo)electrochemical reactions can be categorized into gas-evolving reactions (GERs) and gas-consuming reactions (GCRs).[3] GERs include hydrogen evolution reaction (HER) and oxygen evolution reaction (OER), which can occur concurrently at the cathode and anode for overall water splitting. GCRs consist of oxygen reduction reaction (ORR) to H_2O/H_2O_2 and nitrogen reduction reaction (NRR) to NH_3 (**Figure 1**). Notably, regarding NRR, due to the high solubility of ammonia gas in water (32 g per 100 mL at 25 °C), NH_3 formed during reaction will quickly dissolve in the aqueous electrolyte. However, in addition to the consumed CO_2 and CO gases during carbon dioxide reduction reaction (CO_2RR) and carbon monoxide reduction reaction (CORR), there could be gases and/or liquids produced using different catalysts during CO_2RR/CORR. Therefore, CO_2RR and CORR usually involve both GER and GCR (**Figure 1**). To date, extensive research efforts have been devoted to understanding the catalytic mechanisms and in particular the influences of the morphology and composition of the electrode on the reaction efficiency.[4-11]

Chem. Soc. Rev., 2021,50, 10674-10699, https://doi.org/10.1039/D1CS00258A

During (photo)electrocatalytic GERs in aqueous electrolyte, gas bubbles are formed on the surface of (photo)electrodes. The aggregation of these bubbles between catalysts and electrolyte will not only reduce the availability of exposed active sites, but also severely hinder mass transport in the liquid phase, thus slowing the charge transfer and resulting in inferior (photo)electrocatalytic activity and stability. Therefore, efforts towards industrial-scale GER have focused on achieving rapid release of the formed gas bubbles in order to retain the activity of the (photo)electrode.[12] In contrast, during GCRs, the (photo)electrode design should enable unobstructed gas-diffusion pathways to continuously supply sufficient gas reactant to the catalytic sites. This will preferably create abundant gas/electrolyte/catalyst three-phase contact lines with water usually serving as the proton source.

Taking into account the influence of the gas-liquid-solid interface on (photo)electrocatalytic processes, understanding and exploiting material wetting properties may provide solutions to outstanding problems (*i.e.* boundary layer limitation, limiting current etc.) in the (photo)electrode design. Just as the catalytic systems for water splitting and NRR are inspired from Photosystem II and enzyme nitrogenase respectively,[13, 14] nature-inspired design principles of superwettable materials may also shed light on furthering the development of novel (photo)electrodes.[15] Preliminary studies have already shown that the adhesion and transport behaviors of gas layer/bubbles near/on/inside the (photo)electrodes are controllable by tailoring their compositions, morphologies and 3D structures.[16-20]

In this review, we focus on the recent progress of wetting-regulated gas-involving (photo)electrocatalysis. The fundamentals of bioinspired (super)wettability and the potential for (photo)electrode designs are first introduced. Afterward, bubble adhesion and transport behaviors in smooth and porous media are discussed. In the subsequent sections, the design strategies towards improved catalytic performance for (photo)electrodes with related

experimental evidences in GERs and GCRs are summarized. In the last section, we discuss the open challenges and propose potential directions for future research.

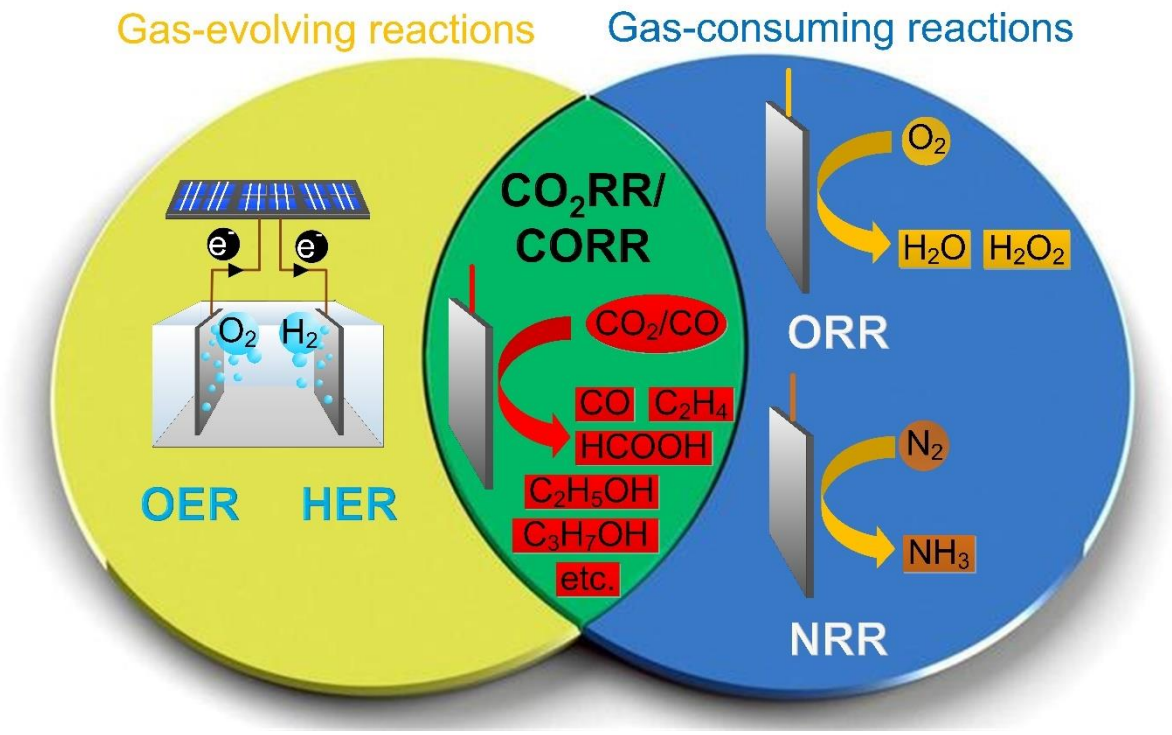

Figure 1. Categories for (photo)electrocatalytic gas-involving reactions.

2. (Photo)electrode Designs taking Inspiration from Superwettability in Nature

The presence of bubbles on electrodes influences the efficiency of (photo)electrocatalytic gas-involving reactions. In GERs, release of bubbles is preferential as they block active sites.[21, 22] To minimize the loss of catalytic activity, understanding and control of the shape and adhesion of bubbles on electrodes is required.[23-25] In GCRs, bubble entrapment is preferential as gases serve as the reactant.[26-28] Therefore, enabling and optimizing plastron (air layer) durability and bubble-uptake is desired.[29] The interaction of electrodes and bubbles depends on many parameters, such as surface roughness, material and liquid properties, bulk mixing, and even applied voltage.[30, 31] Depending on operating conditions, the bubble/drop shape may change. Our ability to grasp and control the fundamentals of bubble mobility will guide the design of future electrode materials and morphology in order to enhance process yields and efficiency.

Wetting is conventionally quantified by the contact angle, θ (**Figure 2**). It represents the angle at which a wetting fluid (liquid or gas) contacts a surface.[32] This angle is always defined as the angle between the chord and the circular arc. In the following, surface refers to the electrode surface. The contact line is where the so-termed three-phase meets, *i.e.* air-water-surface contact. At the macroscopic scale, this is represented by drop/bubble velocity. Using water as a probe liquid, surfaces with a θ_{air} < 90° are considered hydrophilic (**Figure 2a**), while those with a θ_{air} > 90° are considered hydrophobic (**Figure 2c**).[32] When submerged, these are also aerophobic (θ_{bubble} > 90°) and aerophilic (θ_{bubble} < 90°) respectively (**Figure 2b,d**).[27, 33-35] Contact angles, however are not uniquely defined. Stationary drops and bubbles can exhibit a range of contact angles. This occurs because the three-phase contact line (line where bubble-liquid-surface meet) may not actually move even when its volume or shape is slightly perturbed (**Figure 2e**). The three-phase contact line remains pinned to the surface[36-39] until a maximum θ_{adv} or minimum θ_{rec} contact angle is reached (**Figure 2e**, shift in second-to-third dotted lines and moving drop, right side).[38-42] Thereafter, the contact line moves (advances or recedes). This dynamic contact angle is thus bracketed by the advancing contact angle, θ_{adv} and the receding contact angle, θ_{rec}.[37, 40]

However, θ_{adv} of θ_{rec} sensitively depend on the degree of pinning, surface roughness and chemical inhomogeneities, and even optical resolution.[36, 43, 44] Moreover, measurements are also influenced by contact line velocity, *i.e.* drop velocity.[45-47] High resolution optical microscopy[39, 45, 48] is known to improve the accuracy of these measurements.

For rough surfaces one distinguishes between different regimes. Here, it is important to note that roughness amplifies wetting. A hydrophobic surface becomes more hydrophobic, whereas a hydrophilic surface becomes more hydrophilic. Moreover, roughness may result in fractional wetting behaviour. With wetting on a rough surface, apparent contact angles (θ^{app}) are observed. Superhydrophilicity represents a superwetting state where θ_{air}^{app} is lower than 5-10°

(**Figure 2f)**. The surface (and its asperities) is completely wetted by the liquid.[49] There is some debate within the community with regards to the importance of the timescale (milliseconds *vs.* seconds) in achieving such low contact angles (superspreading *vs.* hemiwicking).[50-55] The speed and degree of imbibition depends on surface energy and morphology.[53,56] However, such specificity is irrelevant for the field of catalysis due to the timescales involved (minutes to hours). In all cases: when submerged, these surfaces are superaerophobic (**Figure 2g**).[35]

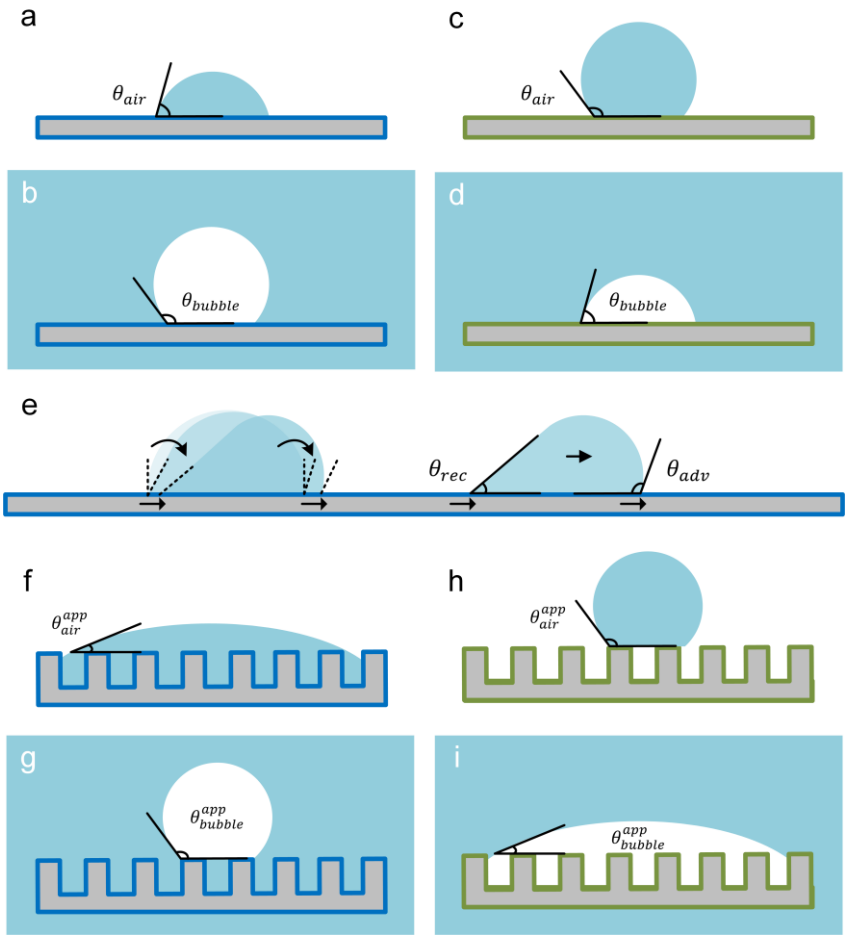

Figure 2. Wettability and Contact Angles (apparent and dynamic). a,b) In-air hydrophilicity and under-water aerophobicity. c,d) In-air hydrophobicity and under-water aerophilicity. e) Drop motion, contact line depinning and advancing/receding contact angles. f,g) In-air superhydrophilicity and under-water superaerophobicity. h,i) In-air superhydrophobicity and under-water superaerophilicity.

Superhydrophobicity (or superoleophobicity/superamphiphobicity for low surface tension liquids) represents a super(de)wetting state where θ_{air}^{app} is higher than 150° and the roll-off

angle (5-10 µL drops) is lower than 10° (**Figure 2h**).[57, 58] Air pockets between the surface and liquid are preserved, culminating in the fractional-wetting state. The solid-water contact areas are defined as a fraction f while the air-water contact areas are defined as the complementary (f-1).[59, 60] In this state, the actual advancing water contact angle ($\theta_{adv,air}^{actual}$) is always close to 180°,[61] because the contact lines moves over fragmented water-solid-air interfaces. When submerged, these surfaces are superaerophilic (**Figure 2i)**.

In the following, we discuss these concepts on natural surfaces. In Nature, the roughness and chemistry of surfaces greatly vary. Consequently, different wetting behaviors exist over a wide spectrum. Such observations have inspired many researchers to investigate natural surfaces in greater detail. The aim is to transfer such concepts to the design of next-generation electrodes (**Figure 3**). For photoelectrodes, natural organisms' anatomical features (*e.g.* moth eyes, butterfly wings, fern leaves, sunflowers) have inspired smart sophisticated architectures and strategies. These features have proven to reduce the loss of absorbed light through reflection while enabling enhanced light harvesting capabilities.[62]

In the context of wetting, variations in surface energy and surface morphologies are commonly found in both land and water plants, potentially providing guidance towards the development of gas-evolving and gas-consuming (photo)electrodes for (photo)electrocatalysis. When electrodes (solid) are submerged, the understanding, control and minimizing of pinning of bubbles on solid will contribute to the design of advanced wetting-regulated electrodes.

Superhydrophilic ($\theta_{air}^{app} \approx 0°$) plants such as the water-absorbing moss (*Sphagnum squarrosum*) employ the presence of micropores (0.2-1 µm) within a sponge-like epidermis (**Figure 3a,e**). These hydrophilic micropores draw in moisture from fog, dew or rain *via* capillary action in order to prevent drying out.[63] When immersed, in-air superhydrophilicity becomes under-water superaerophobicity. When employing superhydrophilicity in electrocatalysis, gas bubbles (hydrophobic entity) tend not to form or stay on electrodes, thus

preserving a high density of catalytically active sites (**Figure 3i,m**).[30, 35] Superhydrophilic electrodes (*i.e.* Ni_2P nanoarrays in **Figure 3i)** are well-suited for gas-evolving reactions (GERs) due to high gas-liquid contact. However, they are not favorable for gas-consuming reactions (GCRs) due to the inhibition of direct wetting.

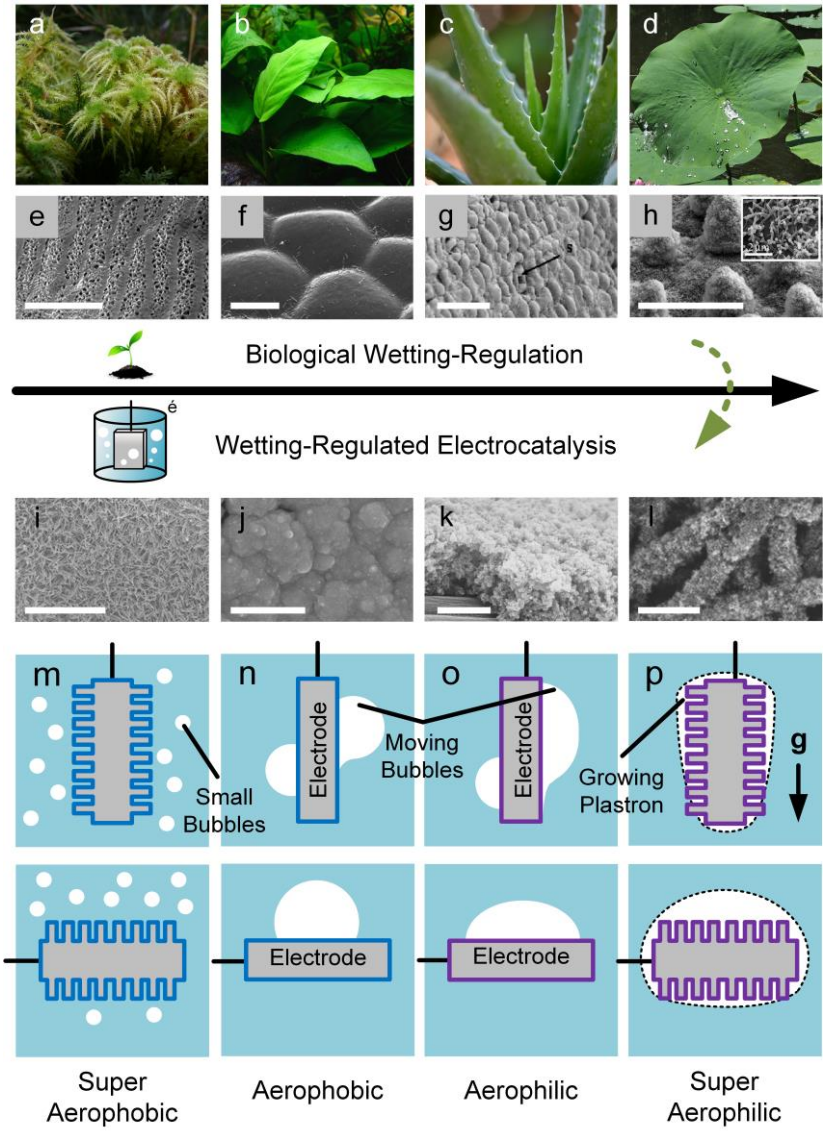

Figure 3. Superwettability in plants adapted to in-air, near-water and underwater-environments and how they may inspire future electrode designs. These include the (a,e) superhydrophilic water-adsorbing moss (Sphagnum squarrosum),[64] (b,f) hydrophilic under-water plant (*Anubias barteri*),[64] (c,g) hydrophobic succulents (*Aloe barbadensis miller*),[65] and the (d,h) superhydrophobic lotus plant (*Nelumbo nucifera*),[64] (g: scale-bar 5 µm, e,f,h: scale-bars 20 µm, inset 2 µm). Their unstructured or structurally-enhanced wettability inspires the development of immersion applications in electrode designs for (photo)electrocatalytic gas-involving systems. (i) Superaerophobic Ni_2P nanoarrays for HER (scale-bar 50 µm),[66] (j) Pt nanosphere film for HER (scale-bar 1 µm),[67] (k) hydrophobic Au/C gas diffusion electrode for CO_2RR (scale-bar 1 µm),[68] and (l) superaerophilic carbon-nanotube-array electrode for ORR

(scale-bar 20 µm).[69] (m) Superhydrophilic/Superaerophobic electrodes result in the formation of tiny bubbles. (n) Hydrophilic/Aerophobic electrodes result in the formation of small bubbles having higher bubble contact angles. (o) Hydrophobic/Aerophilic electrodes result in the formation of large bubbles having lower bubble contact angles. (p) Superhydro(oleo)phobic/Superaerophilic electrodes result in the formation of a continuous plastron until very large bubbles detach by tearing away from the bulk plastron layer. Top *vs.* bottom panels: Bubble detachment depends on the orientation gravity and the central axis of the bubble, Top (Orthogonal); Bottom (Parallel).

Hydrophilic (θ_{air}^{app} = 10-90°) under-water plants such as the common aquarium *Anubias barteri* have comparatively smooth epidermal surfaces (**Figure 3b,f**). The smooth surface allows for reduced shear with under-water currents, while aiding in the removal of any solid (hydrophobic) contaminants.[70] Hydrophobic (θ_{air}^{app} > 90°) succulent green desert plants such as the *Aloe barbadensis miller*[65] likewise possess smooth hydrophobic epidermal surfaces (**Figure 3c,g**). Like many other desert plants, the thick wax cuticles prevent water loss.[71] The use of hydrophilic (Pt nanosphere film, **Figure 3j,n**) and hydrophobic (Au/C gas diffusion electrode, **Figure 3k,o**) electrodes under immersion results in the corresponding aerophobic and aerophilic states when in contact with bubbles. The electrode surfaces are wetted. However, the degree of wetting / aerophobicity will result in the adsorption/formation of micro- to milli-metric bubbles. When pinned, bubbles re-orientate on electrode surfaces depending on the electrode's orientation and the action of gravity. These electrode variants are commonly used for both gas-evolving and gas-reacting systems.[27]

Superhydrophobic (θ_{air}^{app} > 150°) on-water plants such as the lotus (*Nelumbo nucifera*)[72] exploit the presence of both micro- and nano-scale protrusions. Water partially rests on air pockets and only partially wets the surface (**Figure 3d,h**).[60]. Due to the reduced contact, liquid adhesion remains remarkably low, thus enabling high mobility of water drops from rain or splashes to clean away solid (hydrophobic) contaminants.[73] For superhydro(oleo)phobic/superaerophilic electrodes (*i.e.* carbon-nanotube-array, **Figure 3l,p**), a plastron layer is typically formed immediately upon immersion.[27] The plastron could be important in GCRs due to the large gas-to-solid contact area provided. However, they are

clearly not the choice for gas-evolving systems due to poor liquid wetting (hence liquid-contact) properties.

Most laboratory-scale electrode configurations typically involve its longitudinal axis aligned parallel with gravity (**Figure 3m-p**, top panel). However, it may also be aligned perpendicular to gravity (**Figure 3m-p**, bottom panel). Therefore, depending on the wettability and actual surface configuration, buoyancy may influence the shape of the bubble on the electrode. In superhydrophilic/superaerophobic electrodes, the ability of the bubbles to escape may scale with buoyant forces moving them off the electrode (**Figure 3m**). For hydrophilic/hydrophobic electrodes, bubbles may adopt asymmetrically-deformed or symmetric profiles (**Figure 3n-o**).[74-76] In superhydrophobic/superaerophilic electrodes, plastron orientation may result in gas-deficient locations (**Figure 3p**, top panel vs. bottom panel).[27, 35] Evidently, the states of extreme superwettability: superaerophobicity and superaerophilicity present the most intriguing wetting properties for further investigation in GER and GCR electrode design.

3. Design of Bubble Transport in Smooth and Porous Media

For the sake of brevity, the influence of liquid saturation, nucleation delay, critical bubble nuclei, and liquid-phase boundary layer effects will not be discussed as this has been covered extensively by a recent review.[77] We begin the discussion with bubbles that have already heterogeneously nucleated and are currently growing.[25, 28] The timescale between nucleation and detachment depends on 1) bubble growth rate, 2) diffusive fluxes, and 1) detachment size,. Therefore, growth-detachment kinetics, akin to reaction kinetics, rely on operating parameters. For instance, in HER, the growth-detachment process takes place in the order of 1-100 s while H_2 bubbles are growing.[78, 79] Notwithstanding quantifiable contributions by the decrease of active sites[79] or concentration potential[32], the presence of bubbles unanimously results in a decrease in electrocatalytic current density (hence by proxy, reaction kinetics). In general,

bubble growth and adhesion processes are commonly known today to directly interfere with electrocatalytic processes.[80]

3.1 Bubble Shape

Bubble shapes depend on the orientation of the electrode with respect to the gravitational force. This is reflected by the Bond (Bo) number, $\frac{\Delta\rho g L^2}{\gamma}$, where $\Delta\rho$ is the between the gas-liquid phases, g is the gravitational constant, L is the characteristic length (radii of curvature), and γ is the surface tension. The Bond number is a dimensionless number that measures the ratio of gravitational forces *vs.* surface tension forces. With a Bo of > 1, gravity influences the shape of the bubble (**Figure 4a,b**).[81] As a bubble grows, the contact line moves.

3.2 Buoyant Forces

Buoyant forces, F_b is one of the primary forces (**Figure 4c,d**) involved in bubble mobility. In a spherical bubble, buoyancy is defined by the displaced liquid, $F_b = \Delta\rho g V$, where V is the bubble volume. Therefore, with a spherical unadhered bubble, the buoyancy is

$$F_{b,sphere} = \Delta\rho g(\frac{4}{3}\pi r^3) \quad (1)$$

where r is the radius of the bubble (non-adhered).[3] With this spherical approximation, force balances such as the Fritz equation[82, 83] allows for an estimation of critical bubble dimensions (See Section 3.5). However, if the bubble is spherical but adhered as a spherical cap (SC, **Figure 4e**),[84] the volume and buoyant force must be re-defined (assuming low Bond numbers),

$$V = \frac{\pi}{3} r_{SC}^3 (2 + cos\theta_{bubble})(1 - cos\theta_{bubble})^2 \quad (2)$$

where r_{SC} is the radius of the spherical cap. r and r_{SC} can be significantly different depending on the local contact angle. Under this approximation,

$$F_{b,SC} = \Delta\rho g \frac{\pi}{3} r_{SC}^3 (2 + cos\theta_{bubble})(1 - cos\theta_{bubble})^2 \quad (3)$$

The volume is defined based on the polar angle (α), which is equals to the bubble contact angle, $\theta_{bubble} = 180° - \theta$. This spherical cap approximation is analytical and can be easily applied to improve the accuracy of estimates (**Figure 4e**). For a rough surface, the θ_{bubble}^{app} must be determined. θ_{bubble}^{app} is found between the bubble's advancing (θ_{bubble}^{adv}) and receding (θ_{bubble}^{rec}) contact angles (**Figure 4c,d**). However, if bubbles are distorted (laterally or vertically) due to high Bond numbers (Bo >> 1), the actual volume should be defined numerically in 3D due to the biaxial asymmetry involved.[85]

3.3 Vertical Adhesion

When gravity acts parallel to the central axis of the bubble-on-surface, it adopts the shape of a spherical cap. To detach the bubble from the surface, the adhesion force needs to be overcome. A bubble detaches from a surface in an analogous manner to vertical drop-from-surface detachment. Here, the upper limit for vertical adhesion force (bubble-to-plate)[86, 87] is defined by

$$F_{v,adh} = \pi D\gamma \, sin(\theta_{rec}^{bubble}). \quad (4)$$

where D is the diameter of the circular area where the bubble is in contact with the electrode.

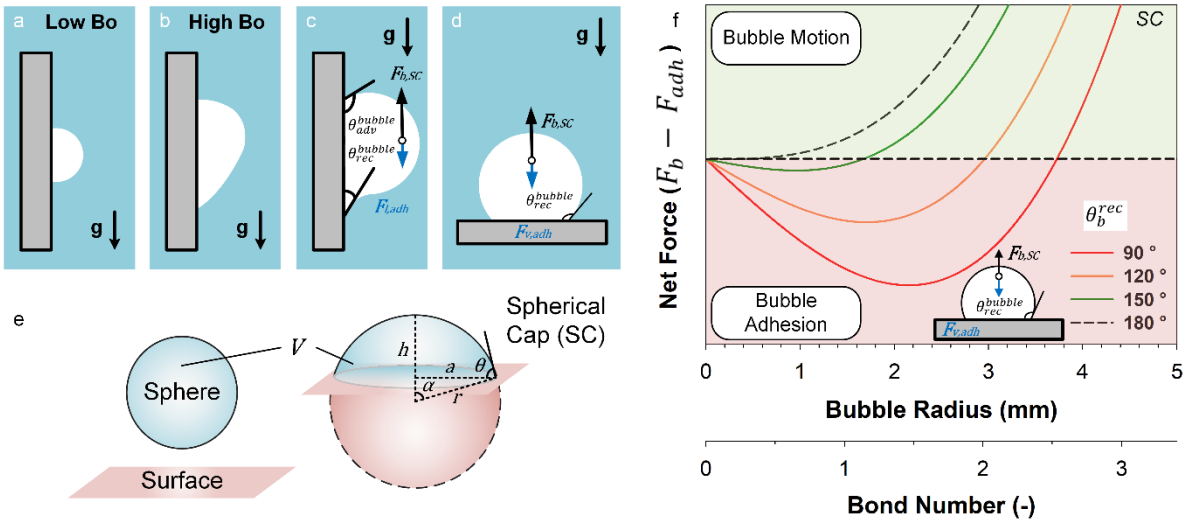

Figure 4. Mechanism of bubble transport on flat and structured surfaces. (a-b) Influence of bubble size on Bond number and gravitational influence on bubble shape. (c-d) Force balance represented on a bubble (buoyancy) adhered to a (c) vertical plate (lateral adhesion, $F_{l,adh}$) and (d) horizontal plate (lateral adhesion, $F_{v,adh}$). Computation of effective buoyancy

and adhesion (contact line) corrected by (e) the spherical cap approximation (vs. sphere approximation). (f) The case for symmetric bubble detachment (vertical adhesion, bubble-on-plate) is computed based on bubble radii / Bond number (x-axis) and θ_{rec}^{bubble} (lines) *vs.* net force (y-axis), $F_{net} = F_{b,SC} - F_{v,adh}$. The spherical cap approximation was applied.

Note that no advancing bubble contact angle, θ_{bubble}^{adv} exists as all contact lines are receding. The case for vertical adhesion of a bubble in water: $F_{v,adh}$ *vs.* F_b is presented in **Figure 4f** *via* a range of θ_{bubble}^{rec}. The threshold bubble size (r) for contact line motion occurs when $F_b > F_{v,adh}$, or a positive $F_{net} = F_{b,SC} - F_{v,adh}$. As the contact line begins to move, the contact line shrinks in size (*i.e.* D decreases), therefore $F_{v,adh}$ decreases further and the contact line motion accelerates. This eventually results in detachment. A negative F_{net} implies that the bubble remains pinned to the surface while buoyant forces influence the bubble shape and apparent contact angle. This behavior is commonly observed when physically manipulating soft materials such as drops or bubbles.[23] Readers should note that the computation of $F_{v,adh}$ in **Figure 4f** is an upper bound because pinning, necking and rupturing contributions may result in easier detachment of the primary bubble. In these cases, a small satellite bubble may remain on the surface (See Section 3.5). While bubbles on aerophobic surfaces likely detach with a moving contact line (spontaneously decreasing D), bubbles on aerophilic surfaces may not have an actively moving contact line. The latter eventually results in pinch-off (See Section 3.5). Realistically, most real-world surfaces (flat) are comparatively hydrophilic (θ_{air}^{app} = 30-90°)[88, 89] which results in an aerophobic behavior (θ_{bubble}^{app} = 90-150°) when underwater.

3.4 Lateral Adhesion

When gravity acts orthogonally to the central axis of the bubble, the contact angles at the top and bottom differ, *i.e.* asymmetrical bubbles (**Figure 4c, Figure 5a,b**). During bubble motion, the resulting dynamic bubble contact angles ($\theta_{adv}^{bubble}/\theta_{rec}^{bubble}$) are given by the relative local

aerophobicity of the electrodes involved. Lateral movement of a bubble on a surface is analogous to lateral drop-on-surface motion. The adhesion force (bubble-to-plate) involved is defined by the lateral adhesion force,[42, 90, 91]

$$F_{l,adh} = kw\gamma\,[cos(\theta_{rec}^{bubble}) - \cos(\theta_{adv}^{bubble})] \quad (5)$$

The k-factor depends on the shape of the three-phase contact line (*i.e.* $k \approx 1$ for a circular contact line)[90, 92, 93] and w is the width of the drop. With this revised force balance, a similar computation of effective forces per **Figure 4f** can also be performed. The bubble starts moving when $F_{b,SC} > F_{l,adh}$.

3.5 Pinch-off and Necking

During both vertical and lateral bubble detachment, the potential for necking and partial bubble/drop pinch-off exists.[77, 94] Lateral detachment mechanisms will require numerical solutions due to the non-radially-symmetric bubble profile.[85, 95] However, the vertical detachment mechanism may be solved analytically after corrections. Pinch-off occurs when part of the bubble contact line is pinned while the gradually growing bubble increases sufficiently in size. This results in a vertical neck, where the region between the primary bubble and the pinning site thins, forming a dumbbell-shaped geometry. The bubble eventually splits, giving rise to a large primary bubble and a smaller satellite bubble.[94] Forces involved during this process is dominated by the formation and the critical diameter of the neck, D_{neck} (before spontaneous breakage). Without necking, the critical radius, r_{crit}, for bubble detachment may be computed *via* a force balance between spherical-approximated buoyancy, F_b and $F_{v,adh}$, giving the Fritz's equation.[82, 83]

$$r_{crit} = \left(\frac{3D\gamma sin\,(\theta_{rec}^{bubble})}{4\Delta\rho g}\right)^{1/3} \quad (6)$$

With necking, a simple correction from contact diameter, D to necking diameter,

$$D_{neck}.r_{crit,neck} = \left(\frac{3D_{neck}\gamma sin\,(\theta_{rec}^{bubble})}{4\Delta\rho g}\right)^{1/3} \quad (7)$$

While Fritz's equation may be used, the spherical cap approximation (see above) may be applied.

3.6 Porous Surfaces

In efforts to increase the net effective surface area (hence active sites) per volume of electrode material, porous electrodes are often favored in both GERs and GCRs. This increases the net yield per gram of electrode material (which can be costly), thus providing an economical edge. On nano- and micro-structured electrodes, the configuration of wetting becomes superhydrophilic/superaerophobic (**Figure 5c**) and superhydrophobic/superaerophilic (**Figure 5d**) respectively. In the latter, bubbles are more likely to be absorbed into the plastron[96] for reaction while bubble production is severely hindered due to the non-wetting condition. Bubble-to-plastron coalescence takes place over very small timescales (~10-1000 ms) and is likely not the limiting step.[97, 98] Bubbles contacting superaerophobic electrodes do not merge and thus exhibit no coalescence dynamics. Therefore, superaerophilic are preferred for GCRs.

Chem. Soc. Rev., 2021,50, 10674-10699, https://doi.org/10.1039/D1CS00258A

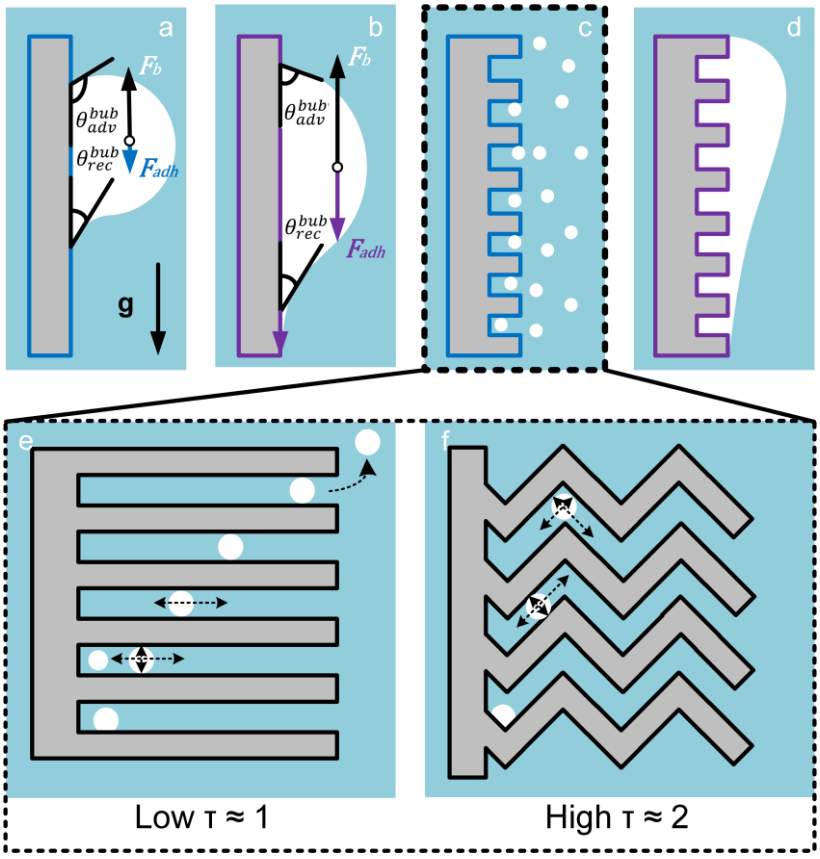

Figure 5. (a) Hydrophilic/Aerophobic surfaces exhibit lower adhesion compared to (b) Hydrophobic/Aerophilic surfaces, thus requiring smaller bubble sizes for detachment. Structured surfaces exist as (c) superhydrophilic/superaerophobic and (d) superhydro(oleo)phobic/superaerophilic variants. In the latter, a (d) thick plastron forms, and any bubble detachment relies on tearing from the primary plastron, which is often unfavorable for GERs. However, they are particularly proficient (albeit durability considerations) for GCRs. Alternatively, (c) superhydrophilic/superaerophobic surfaces may (e) release or (f) entrap bubbles depending on surface structuring (tortuosity, τ). 2D models are depicted for simplicity: Low surface tortuosity would allow for smoother bubble escape compared to higher surface tortuosity.

Electrode material optimized for wetting-enhanced GERs (low $F_{adh}/\ F_b$ ratio) often result in the formation of tiny bubbles (**Figure 5e,f**). However, the ability of a tiny bubble in navigating out of the porous / nano-micro-structured surfaces[30] often relies on the tortuosity factor, τ of the porous electrode and the surface-to-gravity orientation. Tortuosity is defined by $\tau = \frac{C}{S}$, or the arc-chord ratio (≥ 1): the ratio of the length of the curve (C) to the distance between its ends (S). This parameter constrains how the random walk of a bubble will escape the porous network (or not) (**Figure 5e,f**). Therefore, the time of escape, t scales to the n-step

dependent probability $p(n)$ towards which the preferential direction is taken. *i.e.* a small τ, a small n, and $p(n) \approx 1$ guarantees the fastest escape. In reality, $p(n)$ includes contributions from the gravitational constant (and direction), collision with other bubbles,[97] wall adhesion,[28] which are factors that will heavily influence the process beyond simple Brownian forces.

We believe that future design of superaerophobic porous electrodes will entail theoretical and experimental mapping (*i.e.* tomography) of surface tortuosity. Model geometries can also be pre-defined using additive manufacturing methods such as 3D-printing[99] to further improve our understanding of gas-evolving electrodes.

4. Gas-involving (photo)electrocatalysis

4.1 Electrochemical HER

Hydrogen gas bubble nucleation behaviors are affected by the electrode materials, which results from their different wettability. Moreover, electrode morphology and gas diffusion layer thickness are also related to the bubble nucleation on electrodes.[100] Liu *et al.* investigated the individual hydrogen bubble nucleation on flat electrodes, namely polycrystalline Pt, Au and MoS_2, using scanning electrochemical cell microscopy with a single channel pipet.[101] Based on stochastic bubble nucleation measurement and finite element simulation, it was suggested that the threshold of surface H_2 concentration for bubble nucleation is ~218, ~137 and ~157 mM on Pt, Au and MoS_2 electrodes, respectively. Moreover, it was also discovered that the surface faceting of polycrystalline Pt is not correlated with the bubble nucleation behavior. Therefore, one of the strategies is to modify the electrode materials thus adjusting their wettability for facile bubble detachment. For instance, iron ions were irradiated on the surface of Bi_2Te_3 nanosheets to tune the Bi_2Te_3 surface from hydrophobic to hydrophilic, which facilitated the release of hydrogen bubbles from the electrode surface and rapidly exposed the active sites.[102] In addition, varying the conditions during phosphidation process of $Ni(OH)_2$

also led to a range of wettability for the HER catalyst Ni_2P, showing water contact angles ranging from 21° to 79°.[103] The most hydrophilic electrode demonstrated the highest electrochemically active surface area (ECSA)-normalized current density, indicative of its superior intrinsic activity of the catalytic sites.

Another strategy is to optimize the morphology of the electrode to improve its hydrophilicity/aerophobicity. It is worth noting that this strategy is feasible only if the catalyst material is intrinsically hydrophilic/aerophobic. Further increasing the surface roughness of hydrophilic/aerophobic electrode can give rise to superhydrophilicity/superaerophobicity. Compared to CoS_2 film, CoS_2 microwire (MW) and nanowire (NW) arrays were superior in facilitating H_2 bubble convection away from the electrode surface (**Figure 6a**).[22] Consequently, the increased surface texture not only decreased the overpotential required to achieve a target current density (**Figure 6b**), but also improved the long-term stability for HER (**Figure 6c**). This was ascribed to the rapid bubble detachment, which prevented the H_2 bubbles from accumulating and damaging the catalyst, as commonly occurred for the CoS_2 films. Later on, superaerophobic Ni_2P nanoarrays (**Figure 6d**) and N-doped tungsten carbide (**Figure 6e**) nanoarrays have also been developed with excellent HER activity.[66, 104] The bubbles on N-doped tungsten carbide (N-WC) nanoarray electrode were much smaller and detached much faster than those on the other electrodes (**Figure 6f**), which was in line with its largest bubble contact angle (**Figure 6g**) and lowest bubble adhesion force of <1.2 μN. In addition, other hydrophilic/aerophobic electrocatalysts with various morphologies have been developed for efficient HER, such as superaerophobic pine-shaped Pt nanoarrays (-0.04 V vs. RHE at ~10 mA cm^{-2}),[67] MoS_2 nanoflakes (-0.23 V vs. RHE at ~10 mA cm^{-2}),[105] Ni nanoparticles-decorated NiMoN NW arrays (-0.037 V vs. RHE at 10 mA cm^{-2}),[106] WS_2 nanoparticles-modified graphene nanohills (-0.18 V vs. RHE at ~10 mA cm^{-2}),[107] Ni–Mo alloy nanosheets (-0.035 V vs. RHE at 10 mA cm^{-2}),[108] Ni-Zn nanosheet arrays (-0.068 V vs. RHE at 10 mA cm^{-}

^{2}),[109] aerophobic dendritic Ni_5P_4 nanostructures on copper foam (-0.09 V vs. RHE at 10 mA cm^{-2}),[110] superhydrophilic amorphous Co–B–P nanosheets (-0.042 V vs. RHE at 10 mA cm^{-2}),[111] and MoS_2 hierarchical wrinkles (-0.225 V vs. RHE at 10 mA cm^{-2}).[112]

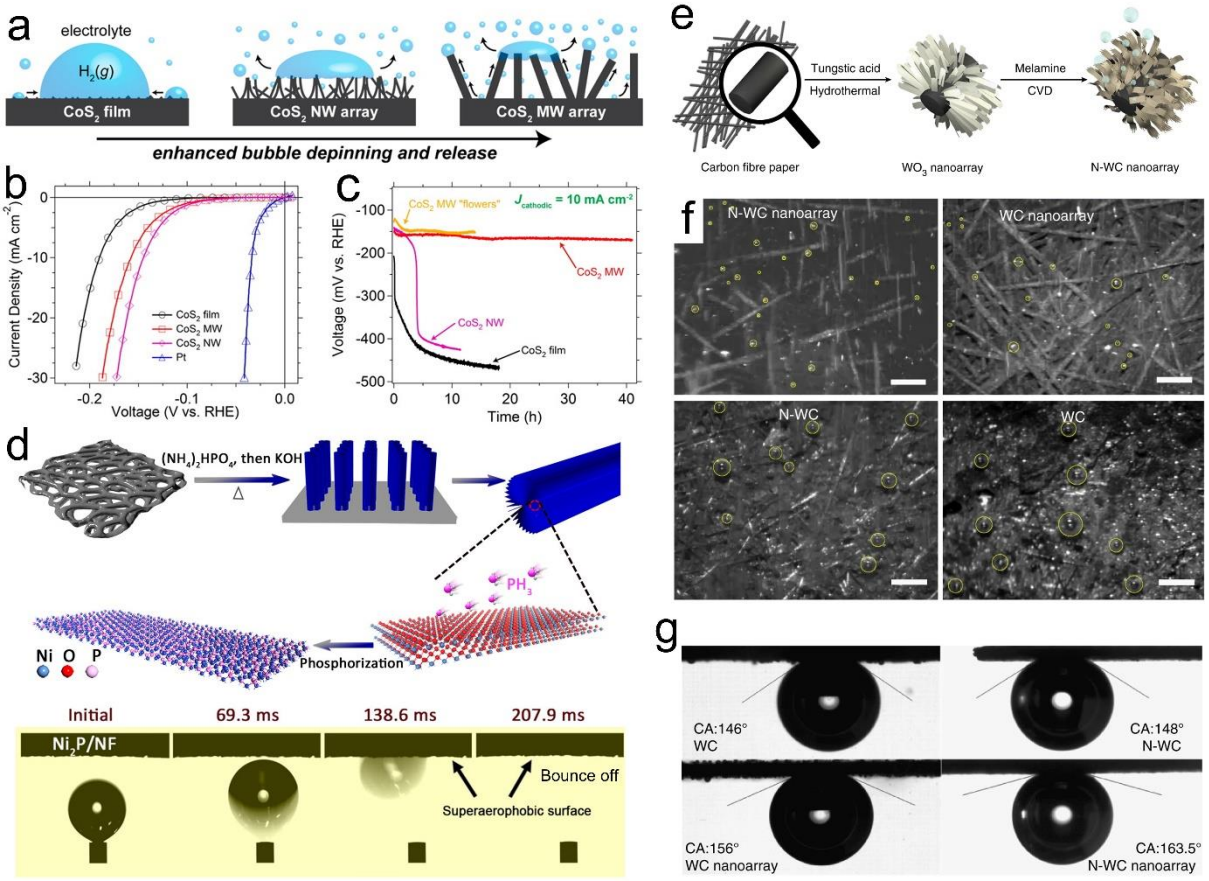

Figure 6. (a) Schematic depictions of CoS_2 MWs and NWs bursting the larger H_2 bubbles that commonly pin on the surface of CoS_2 film. (b) Polarization curves for CoS_2 film, NW, and MW electrodes. (c) Long-term stability tests for CoS_2 film, NW, and MW electrodes. Reproduced with permission.[22] Copyright 2014, American Chemical Society. (d) Schematic illustration of the synthetic process for Ni_2P nanoarrays and digital images of H_2 bubbles on the nanoarray electrode. Reproduced with permission.[66] Copyright 2019, American Chemical Society. (e) Schematic illustration of the synthetic process for N-doped WC nanoarrays on carbon fiber paper. (f) Snapshots of bubbles detaching from different electrodes at −0.2 V vs. RHE. Scale bar is 100 μm. (g) Bubble contact angles on various electrodes of WC, WC nanoarray, N-WC, and N-WC nanoarray. Reproduced with permission.[104] Copyright 2018, Springer Nature.

The third strategy towards rapid release of H_2 bubbles is to take advantage of specially designed electrode structures for efficient bubble transport. This strategy is independent on the wettability of the electrode materials. For example, an aerophilic cone-shaped Cu electrode was fabricated with the adhesive force of 167 ± 14 μN to gas bubble and the bubble contact

angle of 117± 4° (**Figure 7a**).[113] However, the generated H_2 bubbles during HER can be timely removed via efficient and directional transportation from tip to the base (**Figure 7b**). Further integrating the base of electrode with a superaerophilic sponge, which exhibited excellent properties of efficiently absorbing and releasing gas bubbles, can realize the collection of generated H_2. The bubble movement is driven by a Laplace pressure gradient (ΔP) on the aerophilic conical electrode due to the larger Laplace pressure on the tip-side than that on the base-side. Moreover, deposition of a specially designed overlayer on the electrode surface can also facilitate the elimination of H_2 bubbles, which in principle can be applied to virtually any electrode surface (**Figure 7c**). A series of highly porous superaerophobic hydrogels have been prepared by cross-linking M13 bacteriophages through a condensation reaction with glutaraldehyde (**Figure 7d**).[35] This virus was chosen as the building block due to its inherent nanofibrillar structure, hydrophilicity, and high stability under various conditions. Amongst these hydrogels, the optimum one demonstrated an air-contact angle of 159° and corresponding air-sliding angle of 1° (**Figure 7e**). This hydrogel was subsequently used to modify Pt electrode for HER, which resulted in more efficient elimination of adhered H_2 bubbles than bare Pt (**Figure 7f**). The current densities were significantly improved especially at higher potentials where more H_2 bubbles were formed and attached on the electrode surface (**Figure 7g**).

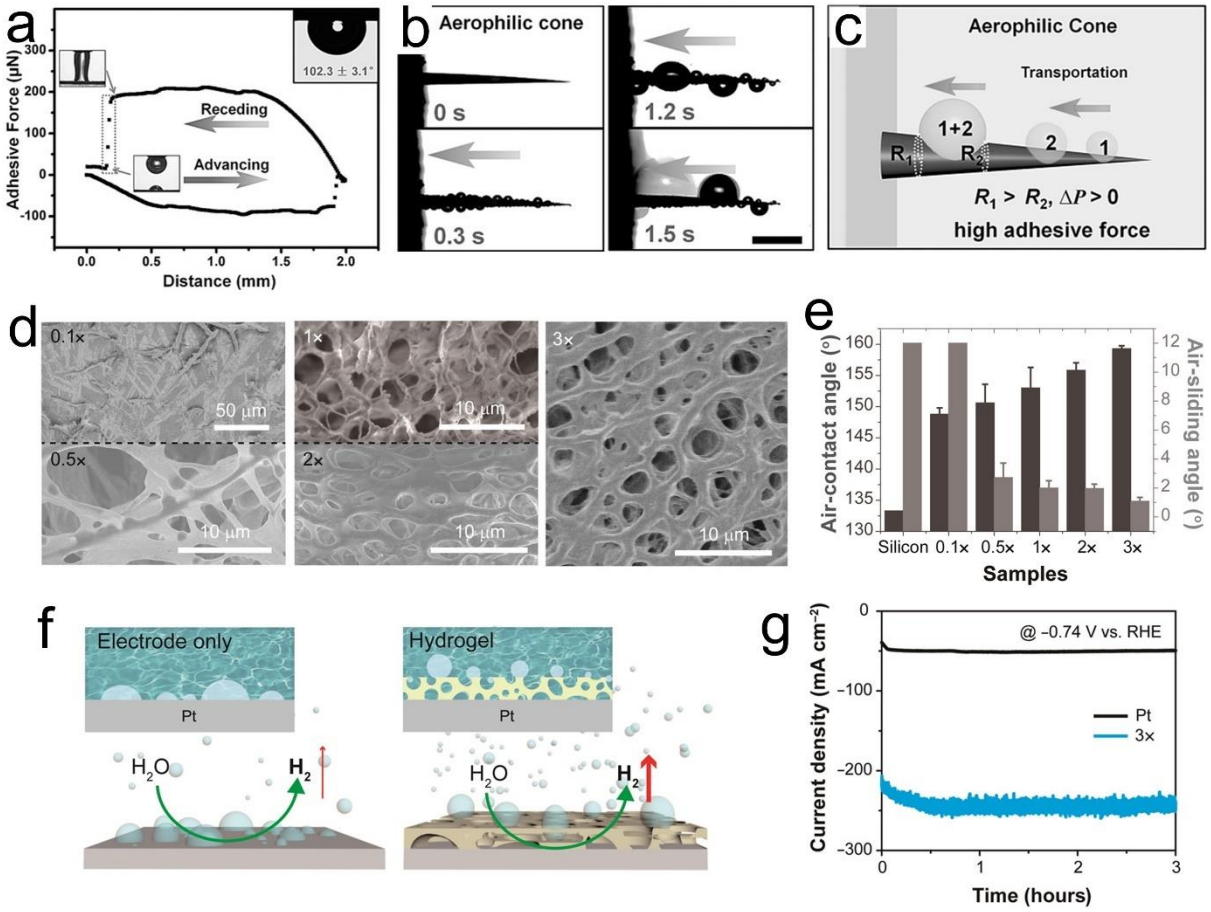

Figure 7. (a) Wetting state/contact model of aerophilic copper surface to gas bubbles. (b) In situ observation of HER on aerophilic cone electrode. Scale bar is 2 mm. (c) Schematic demonstration of H_2 bubbles' behavior on aerophilic copper surface. Reproduced with permission.[113] Copyright 2016, Wiley-VCH. (d) SEM images showing the morphologies of cross-linked viral hydrogels. (e) Comparison of aerophobicity for various hydrogels. (f) Schematic illustrations for the electrochemical HER performance of Pt electrodes with and without the superaerophobic hydrogel. (g) chronoamperograms Pt electrodes with and without the modification with the superaerophobic hydrogels. Reproduced with permission.[35] Copyright 2020, American Association for the Advancement of Science.

4.2 Electrochemical OER

Catalysts for electrochemical OER can be generally categorized into molecular catalysts and heterogeneous catalysts. Regarding molecular OER catalysts, a considerable fraction of them undergo changes during the electrochemical processes.[114] To address this issue, stabilization strategies have been applied to immobilize molecular catalysts on solid surfaces.[115-117] There are three different immobilization strategies, namely covalent bonding,[118, 119] physical interactions,[120, 121] and direct encapsulation.[122, 123] Amongst them, hydrophobic interaction is

one of the physical adsorption-based immobilization methods. Specifically, hydrophobicity of the coordinating ligands can significantly influence the surface-immobilization process and consequently the activity and stability of the molecular OER catalysts. By investigation on a library of molecular OER catalysts based on the Co-complexes of tris(2-benzimidazolymethyl)amine with tailored hydrophobicity (**Figure 8a,b**), it was found that more hydrophobic coordinating ligands with longer alkyl chains or fluorinated groups led to decreased overpotentials, enhanced turnover frequencies and long-term stability due to improved immobilization on the substrate surfaces through physisorption (**Figure 8c,d**).[124] Besides physical properties, OER mechanism of molecular catalysts can also be affected by their wettabilities. From the study of supramolecular dimers of $[Ru^{V}O(pda)]^{+}$ (pda = 1,10-phenanthroline-2,9-dicarboxylic acid) and $[Ru^{V}O(bda)]^{+}$ (bda = 2,2′-bipyridine-6,6′-dicarboxylate) complexes, it was found that the directionality of the hydrophobic and hydrophilic units of the catalyst is a key factor for creating efficient O–O bond-forming catalysts.[125] Specifically, regarding the bda complex, the hydrophobic oxo tended to point at another oxo with the bda directed toward water, which favored the I2M mechanism. On the contrary, the hydrophobic oxo of the pda complex was directed toward a more hydrophobic phenanthroline moiety of the pda of another species bearing more stable binding free energy than that of the prereactive dimer, which made the water nucleophilic attack mechanism competitive.

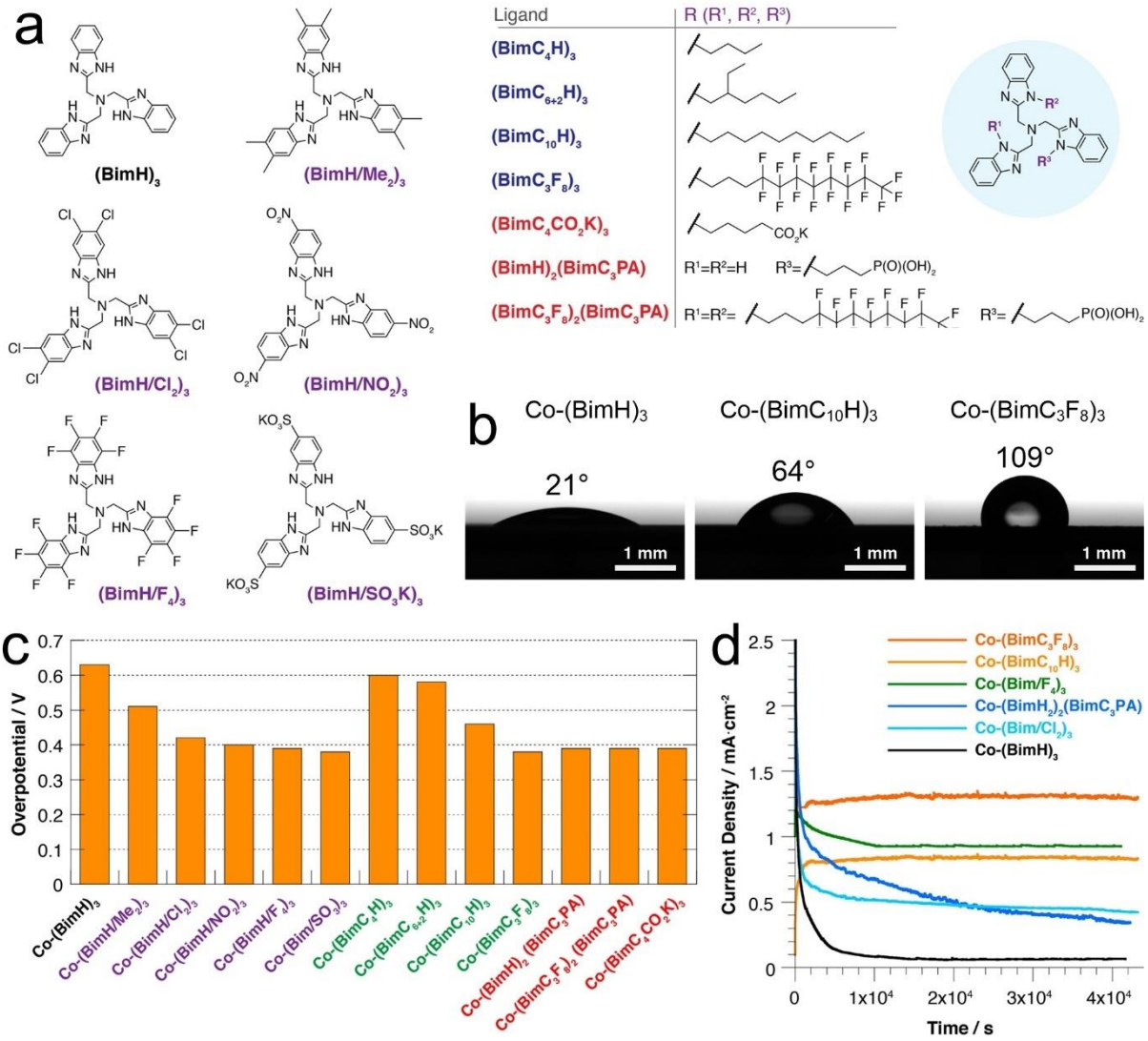

Figure 8. (a) Various tris-benzimidazole Co complexes as OER electrocatalysts. (b) Water contact angles for Co-(BimH)$_3$, Co-(BimC$_{10}$H)$_3$ and Co-(BimC$_3$F$_8$)$_3$ films deposited on a Si wafer. (c) OER overpotentials for various Co complex electrocatalysts. (d) Controlled potential electrolysis traces at 1.91 V vs RHE for selected cobalt complexes. Reproduced with permission.[124] Copyright 2016, American Chemical Society.

In comparison, with respect to heterogeneous OER electrocatalysts, most research efforts have been directed toward enhanced hydrophilicity/aerophobicity of their surfaces, which facilitates O_2 bubble desorption.[126-128] The resulting improved OER catalytic activity is usually attributed to the increased ECSA[129, 130] and decreased interfacial resistance at the catalyst|electrolyte interface during OER.[131] In addition to the surface property, engineering of OER catalyst electrodes into certain structures can also promote efficient transport of evolved gas while maintaining high electrical conductivity, thus resulting in enhanced ECSA-specific

activity. Recently, Kim *et al.* reported a woodpile-structured Ir catalyst containing well-defined macropores (>200 nm) at the inter-wire space with linkage to the inter-layer mesopores (<50 nm) (**Figure 9a,b**).[132] This structure enabled facile transport of evolved O_2 gas bubbles by suppressing coalescence of bubbles from forming larger ones (**Figure 9c**), which was confirmed by scanning electrochemical microscopy (**Figure 9d**) and dynamic light scattering (**Figure 9e**) analyses. Therefore, with both improved ECSA and ECSA-specific activity enabled by the 3D nanostructuring, it demonstrated a 30-fold higher mass activity for OER than conventional nanoparticle-based catalysts in a polymer electrolyte membrane water electrolyzer. Inspired by the breathing process of mammals, a pouch-type alveolus-like nanoporous polyethylene (alv-PE) membrane loaded with Au/NiFeO_x catalyst was fabricated as electrode for OER, whereby the outer membrane touched the electrolyte and the inside pouch was left dry (**Figure 9f**).[133] To assess the impact of the electrode structure on the electrochemical performance, the alv-PE structure was compared with that of the alveolus-like carbon-based gas-diffusion layers (alv-carbon GDL) and flat-PE, exhibiting the highest current density (**Figure 9g**). Its superior performance was ascribed to the following phenomenon. During OER, the newly formed O_2 molecules at the catalyst/electrolyte interface efficiently diffused toward the gas phase inside the pouch, without the additional energy cost of bubble formation, which in turn increased the OER efficiency. This assumption was confirmed by the rarely observed bubbles from the catalyst surface of the alv-PE structure until the applied voltage was increased to 1.65 V (**Figure 9g** [red arrow]).

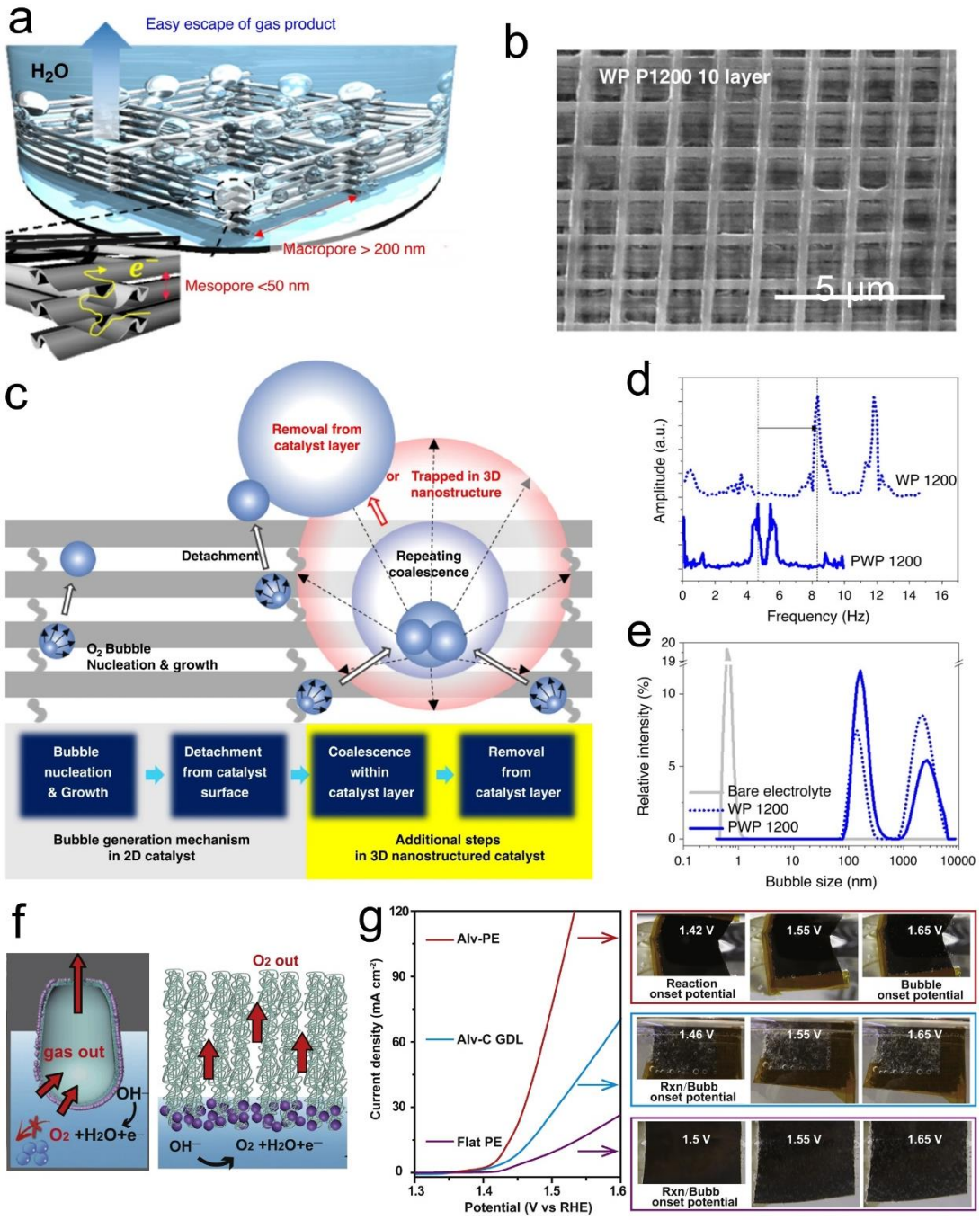

Figure 9. (a) llustration of woodpile-structured Ir as OER catalyst containing mesopores and macropores. (b) Ir catalyst with 10-layer perpendicular-stacking of building block. (c) Schematic illustration of bubble formation and removal mechanism within the 3D-nanostructured electrocatalyst. (d) Fast Fourier transformation amplitude spectra of currents recorded at the tip during scanning electrochemical microscopy analysis. The higher frequency of the peak indicates a faster cycling of formation and detachment of O_2 bubbles. (e) Dynamic light scattering analysis spectra, showing the size distribution of generated O_2 bubbles. Reproduced with permission.[132] Copyright 2020, Springer Nature. (f) Schematic of an alv-PE structure for OER. (g) Linear sweep voltammograms (LSV) curves of Au/$NiFeO_x$-coated membranes with different structures: alv-PE, alv-carbon GDL, and flat-PE. Arrows indicate photographs of their corresponding surfaces with O_2 bubbles onset potential. Reproduced with permission.[133] Copyright 2018, Elsevier Inc.

Overall water splitting

Similar to HER and OER (*vide supra*), efforts towards rapid bubble release have been focused on enhancing the hydrophilicity/aerophobicity of the electrodes or developing novel electrode structures that can suppress gas bubble coalescence, jamming, and trapping. A straightforward method is to simply couple an aforementioned HER catalyst with an OER catalyst as cathode and anode, respectively, for overall water splitting.[134] In addition, certain electrode materials can be catalytically active for both HER and OER. Shan *et al.* synthesized a hierarchical $CoMoS_x$ catalyst on a nickel foam (NF), which showed superhydrophilicity/superaerophobicity with water-droplet contact angle of 0° and under-water gas-bubble contact angle of 165° (**Figure 10a,b**).[135] Therefore, due to the negligible bubble adhesive force (**Figure 10c**), which resulted from the discontinuous state of the three-phase contact line between bubbles and the hierarchical surface of the electrode, the generated bubbles adhered on electrode surface were tiny in the range of tens of micrometers in size (**Figure 10d**). Following this concept, superaerophobic Fe, Co, Ni, Mo, S-based hybrid nanotube arrays,[136] Cu_3P microsheets,[137] Ni–Co–S–P nanoparticles,[138] urchin-like Al,P-codoped Co_3O_4 microspheres on NF[139] and Ni_3Se_2 nanoforest on NF[140] have been developed as bifunctional catalysts for both OER and HER.

Highly controlled, periodic structures, *i.e.*, 3D printed Ni (3DPNi) electrodes decorated with carbon-doped nickel oxide ($C–Ni_{1-x}O$) have also been reported to catalyse both OER and HER at commercially relevant current densities.[30] The printed lattice structure consisted of a linear array of filaments within each layer with centre-to-centre spacing of 800 μm. There are five stacked layers in total with an individual layer's orientation orthogonal to its underlying layer (**Figure 10e**). Compared to the stochastic porous Ni foam, this periodic structure presented a larger critical bubble size, indicating that the generated gas bubbles are less likely to be trapped in its regular porous medium (**Figure 10f,g**). Simulation showed that a bubble with different

diameters in nickel foam exhibited longer transport time than that in the 3DPNi electrode (**Figure 10h**). The varying pore sizes and tortuous paths of the random porous media Ni foam increased the bubble travel distance. Moreover, these structural features also caused the leading portion of the bubble to regularly encounter the solid network ahead of it. The resulting forces exerted on the bubble by the solid beams counteracted the effect of buoyancy, thus slowing the migration. High-speed camera images confirmed that there were more and considerably larger gas bubbles on the C–$Ni_{1-x}O$/nickel foam electrodes than those on the C–$Ni_{1-x}O$/3DPNi electrodes (**Figure 10i,j**). Additionally, nonwoven stainless-steel fabrics as the conductive substrate decorated with bifunctional iron nickel-layered double hydroxide catalyst also led to a much faster escape rate of gas bubbles and less dragging force for bubble releasing than nickel foam and stainless steel foam substrates.[141]

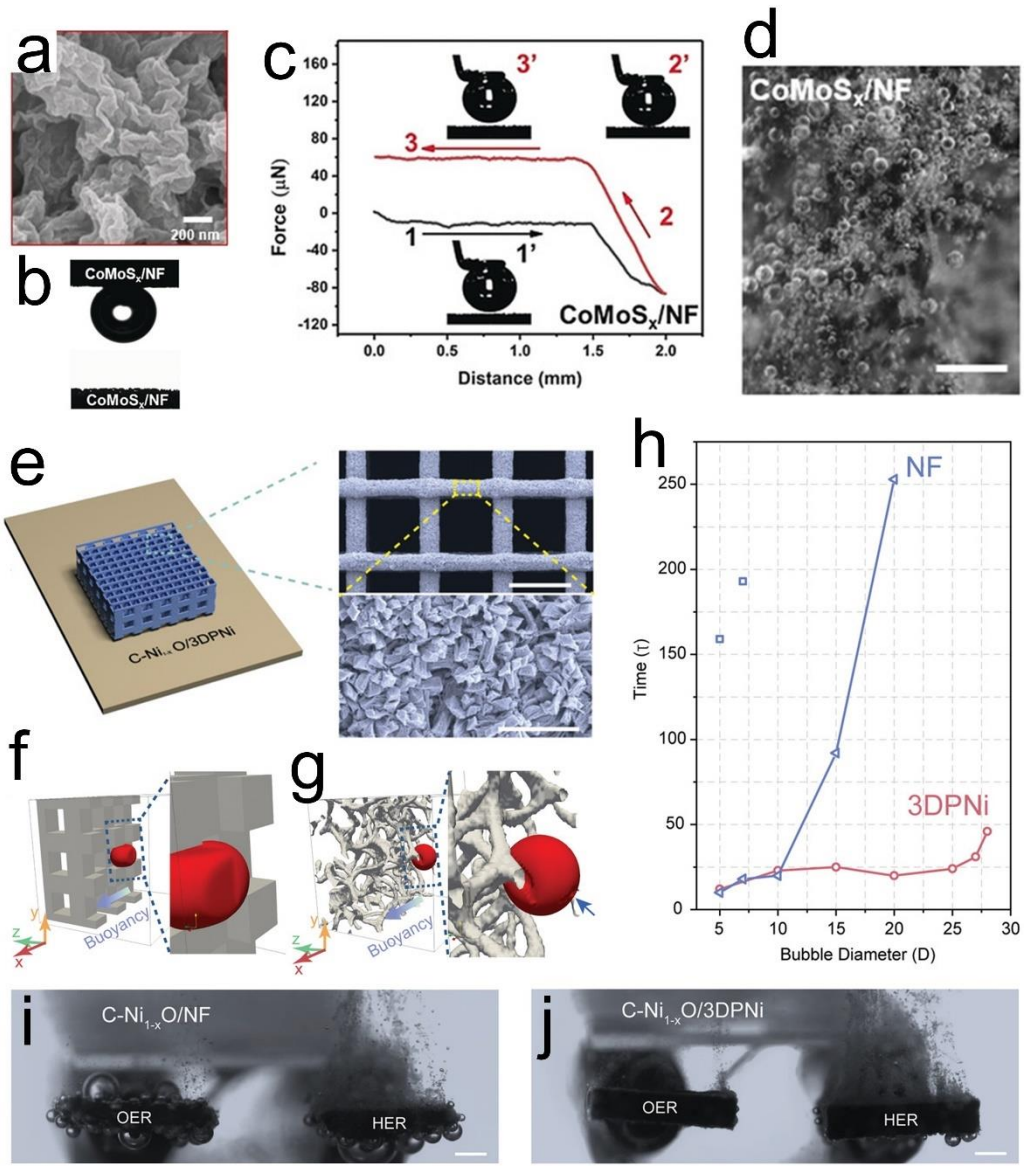

Figure 10. (a) SEM image of $CoMoS_x$/NF. (b) Air-bubble contact angle under water (top) and water-droplet contact angle (bottom) for $CoMoS_x$/NF. (c) Gas-bubble adhesive force measurement of $CoMoS_x$/NF. (d) Digital photograph of bubbles released at the surface of $CoMoS_x$/NF. Scale bar is 0.5 mm. Reproduced with permission.[135] Copyright 2020, Wiley-VCH. (e) Schematic diagram of 3DPNi functionalized with C–$Ni_{1-x}O$ catalyst and its SEM images. Scale bars are 500 and 4 μm, respectively. Simulation frames showing bubble shape during transport in (f) 3DPNi and (g) NF. (h) Relative bubble migration time through 3DPNi and NF as a function of bubble diameter. High-speed camera images collected from the (i) C–$Ni_{1-x}O$/NF and (j) C–$Ni_{1-x}O$/3DPNi electrodes during water electrolysis. Scale bars are 2 mm. Reproduced with permission.[30] Copyright 2020, Wiley-VCH.

4.3 Electrochemical ORR

Electrochemical ORR is a gas-consuming process occurring at liquid/gas/solid interface for energy conversion and storage devices, such as fuel cells and metal–air batteries.[9, 142, 143] In addition to extensive research focusing on the catalyst development, the underwater wettability

plays a crucial role in determining the nature of the liquid/gas/solid interface thus affecting the performance of ORR. To provide a three-phase contact point (TPCP) amongst oxygen, electrolyte and catalyst, the catalytic layer needs to be aerophilic for trapping a thin oxygen plastron layer near the catalyst surface. Based on this catalyst design principle, porous cobalt-incorporated nitrogen-doped carbon-nanotube (CoNCNT) arrays were directly grown on carbon-fiber paper (CFP) followed by subsequent polytetrafluoroethylene (PTFE)-modification (**Figure 11a**).[69] This electrode was denoted as T-CoNCNT-CFP and demonstrated superaerophilic properties with oxygen bubble bursting upon contacting the electrode surface within 42 ms (**Figure 11b**), indicative of a strong interaction between the bubble and electrode. Compared to Pt/C loaded on Teflon-treated carbon fiber paper (Pt/C-TCFP) as electrode, the approaching oxygen bubbles would merge with the plastron layer on T-CoNCNT-CFP electrode and maintain a robust gas film during ORR (the picture on the right in **Figure 11b** and **Figure 11c**). Due to the abundant nanoscale TPCP on the T-CoNCNT-CFP electrode as well as an accelerated gas-diffusion process, it showed better ORR performance in both acid and alkaline electrolyte than Pt/C-TCFP electrode at high current densities, even though the intrinsic activity of the CoNCNTs is inferior to that of Pt/C.[144]

However, more aerophobic state does not necessarily lead to superior ORR performance. There are generally three underwater wetting states for hydrophobic surfaces categorized based on the behaviors at the interface between liquid and solid with increasing hydrophobicity: (1) the liquid completely wetted the solid without trapped air at liquid/solid interface, namely underwater Wenzel state; (2) the liquid partially intruded into the textured solid surface with certain amount of trapped air at the interface, namely underwater Wenzel-Cassie coexistent state; (3) the liquid hardly touched the textured surface, giving rise to a quasi-continuous gas layer over the textured solid surface, namely underwater Cassie state (**Figure 11d**).[29] By investigating three Pt nanoparticles-coated square-pillar-structured silicon wafer electrodes

with subsequent modification of fluorosilane, it was suggested that the superhydrophobic electrode with underwater Wenzel-Cassie coexistent state exhibited the highest ORR catalytic activity (**Figure 11e**), which was attributed to its maximal and stable liquid/gas/solid three-phase interface that was favorable for gas-diffusion.[29]

In addition, combination of both aerophilic and aerophobic surfaces in one electrode can also result in excellent catalytic performance for ORR. Li *et al.* reported a Janus electrode with an aerophilic side and aerophobicity for the other side by partial modification of aerophobic nitrogen-doped carbon nanotube arrays with PTFE (**Figure 11f**).[145] The aerophilic side showed a gas bubble contact angle of 23 ± 2° (**Figure 11g,i**). In contrast, the aerophobic side allowed quick bubble penetration behavior from the aerophobic to aerophilic side (**Figure 11h,j**). Therefore, the Janus electrode with opposite wettability on adjacent sides maintained stable O_2 gas reservoir at the aerophilic side while shortening O_2 diffusion pathway to reach the catalyst at the aerophobic side, thus resulting in comparable ORR performance with Pt/C catalyst (**Figure 11k**) and outperforming merely aerophilic or aerophilic electrode.

Interestingly, superhydrophilic honeycomb carbon nanofibers were also reported as superb catalysts for two-electron ORR performance with a high H_2O_2 selectivity of 97.3% and a mass activity of up to 220 A g^{-1}.[146] By comparing to a less hydrophilic solid carbon nanofiber catalyst with a water contact angle of 38° as control, it was proposed that the superhydrophilicity of the honeycomb carbon nanofiber catalyst contributed to better wetting of the catalyst by the electrolyte, and that the interconnected cavities of its porous carbon skeleton allowed for more effective entrapping of oxygen gas bubbles. Therefore, the three-phase interface was also created with entrapped O_2 and aqueous electrolyte around the defective catalytic sites.

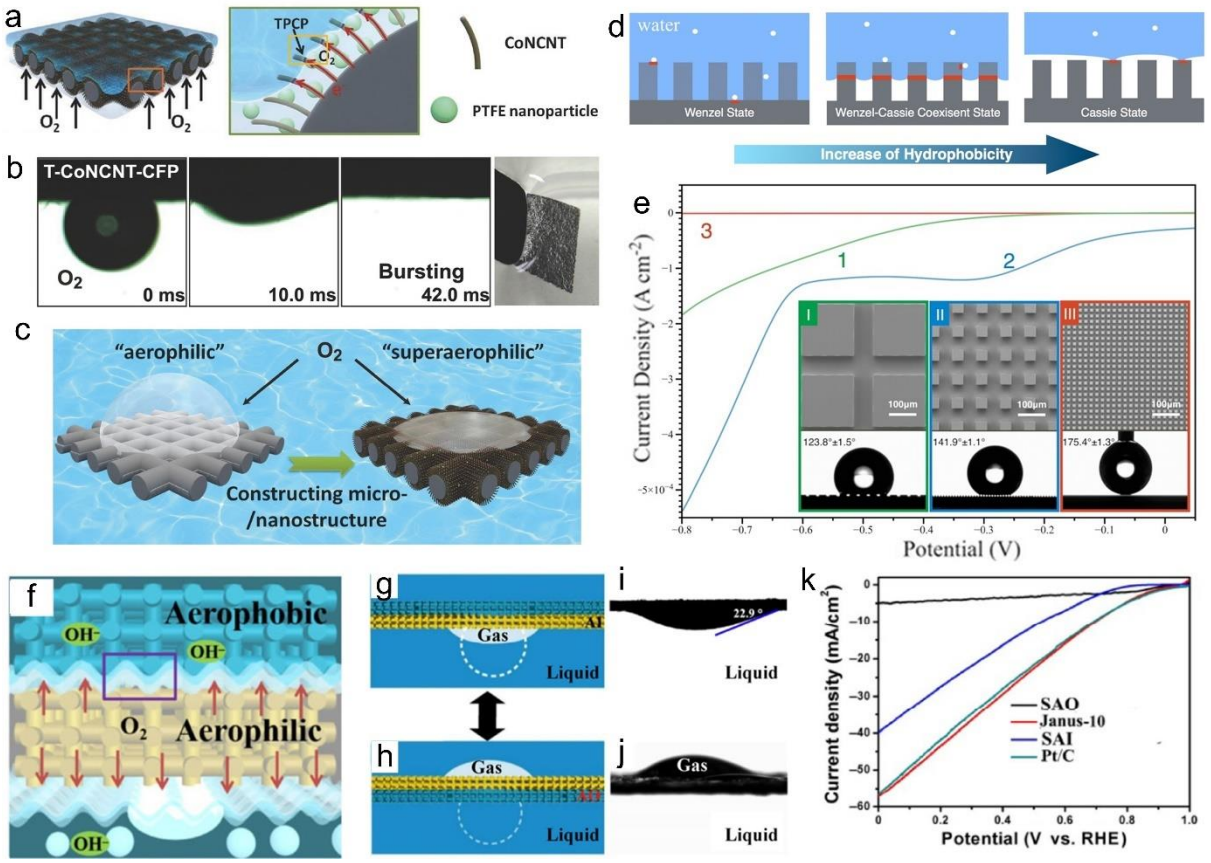

Figure 11. (a) Schematic illustration of the superaerophilic electrode by directly growing CoNCNT arrays on CFP associated with subsequent modification with PTFE. (b) Oxygen-bubble adhesion behavior and optical picture of T-CoNCNT-CFP electrodes in basic electrolyte. (c) Schematic illustration for comparison of the oxygen-bubble adhesion behaviors on aerophilic Pt/C-TCFP and superaerophilic T-CoNCNT-CFP. Reproduced with permission.[69] Copyright 2016, Wiley-VCH. (d) The typical three types of wetting state for a hydrophobic surface in the underwater system, as schematically shown in underwater Wenzel state, Wenzel-Cassie coexistent state, and Cassie state. (e) LSV curves for ORR reaction on three platinum-coated samples. The inset includes SEM images of the morphologies of three kinds of conductive pillar-structured silicon substrates and corresponding water contact angles. Reproduced with permission.[29] Copyright 2016, Wiley-VCH. (f) Schematic illustration of a Janus electrode under ORR conditions. Schematic illustration of the gas bubble behaviour on (g) aerophilic and (h) aerophobic side of the Janus electrode. Gas bubble behaviour on (i) aerophilic and (j) aerophobic side of the Janus electrode. (k) ORR polarization curves of the superaerophobic, Janus, superaerophilic, and commercial Pt/C electrodes in the oxygen-bubbled 0.1 M KOH electrolyte. Reproduced with permission.[145] Copyright 2018, Springer Nature.

4.4 Electrochemical CO_2RR

Electrochemical CO_2RR consists of both gas-consuming and gas-evolving processes, during which CO_2 is reduced with H_2O as the proton source to form mainly $C_{1–3}$ products such as CO (*g*), HCOOH (*l*), CH_4 (*g*), CH_3OH (*l*), C_2H_4 (*g*), C_2H_5OH (*l*) and C_3H_7OH (*l*), as well as H_2 (*g*)

produced by the competing HER.[11] Regarding selective liquid-producing (*i.e.* HCOOH) catalysts, such as Sn-, Bi-based electrodes, it is suggested that their design principles should be similar to those for ORR catalysts. However, taking Au as an example to catalyze CO_2 (*g*) electroreduction to CO (*g*) in aqueous electrolyte, it is necessary to take into account the effects of both gas-consuming and gas-releasing behaviors on the key reaction parameters. The morphological influence of Au electrodes on gas-releasing behavior during CO_2RR was investigated by comparing three electrode morphologies, namely, nanoneedles, nanorods and nanoparticles (**Figure 12a**).[31] The nanoneedles had a smaller bubble departure diameter with a mean value of 23 μm compared to the diameters of 31 and 97 μm for the nanorod and nanoparticle surfaces, respectively (**Figure 12b**). The effervescent generation of small bubbles on nanoneedle surface corresponded to small diffusion thickness, resulting in improved mass transport and intensified CO_2 reduction (**Figure 12c**). Additionally, by comparing a range of Au/C catalysts with the same nanoparticle morphology, the effects of wettability on reactant gas behavior near electrode surface were demonstrated (**Figure 12d**).[68] The Cassie-Wenzel coexistence wetting state with a water contact angle of 107 ± 3° is most favorable for the three-phase-contact CO_2RR system showing fastest reaction rate, highest selectivity towards CO and optimum long-term stability (**Figure 12e**).

Moreover, another effective strategy to improve CO_2RR performance is to design an electrode structure that enables appropriate gas transport both inwards and outwards. Inspired by alveolus structure in mammalian lungs, Au nanoparticles-coated nanoporous polyethylene (nanoPE) membrane was rolled to form a bilayer pouch-type structure (**Figure 12f**).[147] In this structure, the water-impenetrable nanoPE membrane separated the central sealed compartment from the external electrolyte. CO_2 can diffuse into the pores of the nanoPE membrane in the central compartment via the connected inlet. Pinholes on the outer layer enabled ion exchange between interlayer electrolyte and external bulk electrolyte. Compared to Au-coated PTFE-

treated carbon paper and silicon wafer (designated as Au/C and Au/Si, respectively) (**Figure 12g**) as well as hydrophilic bilayer Au/PE pouch-type membrane, it was suggested that both the alveolus-mimicking structure and hydrophobicity contributed to the excellent current density and high Faradaic efficiency for CO production due to the efficient CO_2 access and high local alkalinity.

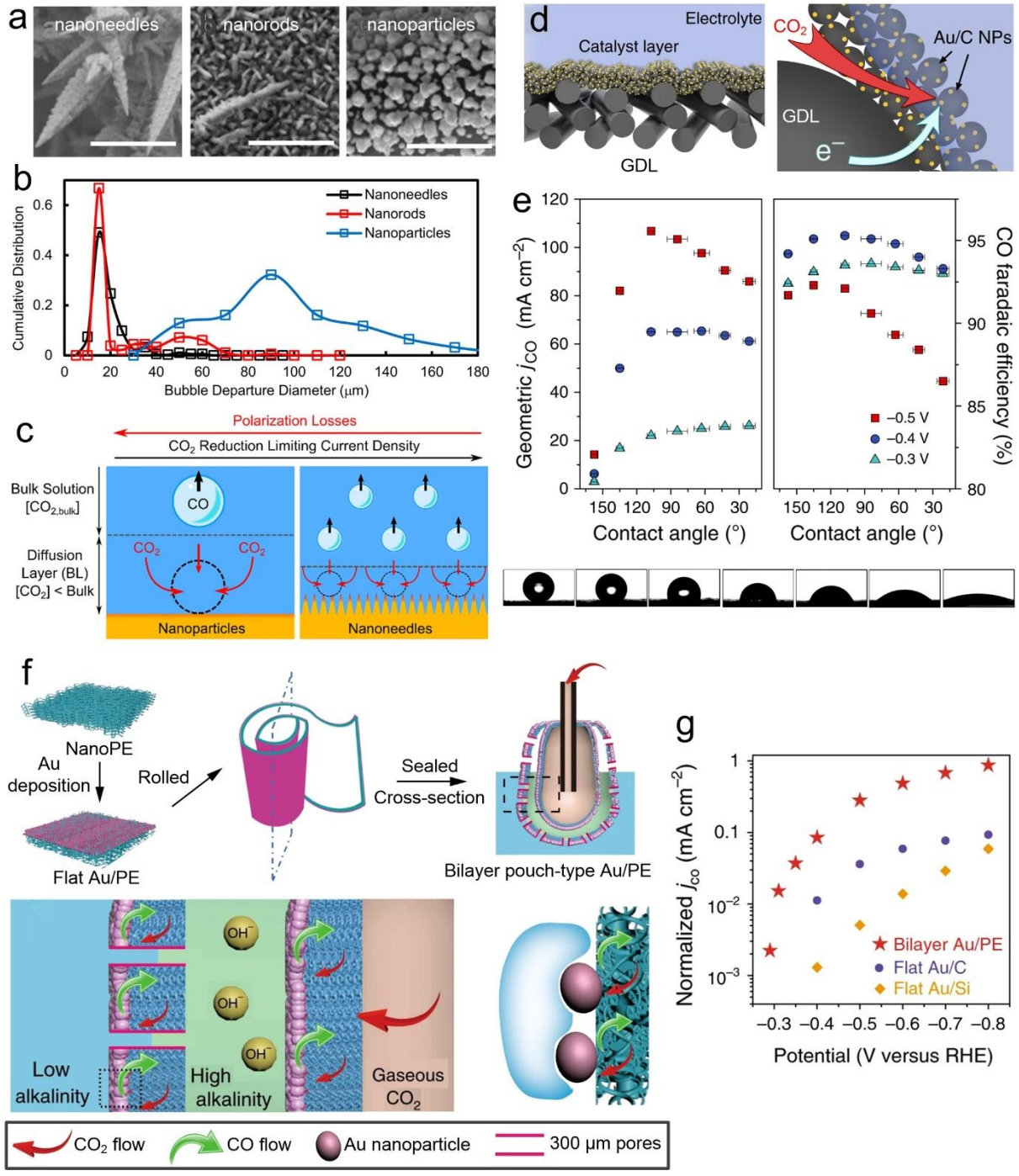

Figure 12. (a) SEM images of nanoneedles, nanorods, and nanoparticles. Scale bars are 5 μm. (b) Cumulative distribution curve of bubble release diameters for Au electrodes with various morphologies. (c) Schematic depicting the influence of electrode morphology on bubble release diameter and the resulting thickness of the diffusion boundary layer. Reproduced with permission.[31] Copyright 2017, American Chemical Society. (d) Schematic illustration of the Au/C electrode and its gas–liquid–solid three-phase interfaces for CO_2RR. (e) Geometric j_{CO}, CO Faradaic efficiency of various Au/C electrodes and photographs of water droplets on each Au/C electrode with different water contact angles. Reproduced with permission.[68] Copyright 2020, Springer Nature. (f) Schematic of fabrication process of Au/PE catalyst for CO_2RR and its detailed structure with three-phase interface between the Au/H_2O/CO_2. (g) Normalized current densities of CO production for a bilayer pouch-type Au/PE, flat Au/C and flat Au/Si.. Reproduced with permission.[147] Copyright 2018, Springer Nature.

Among the electrocatalysts studied to date, Cu is the only known metal that can catalyze the electrochemical CO_2RR/CORR toward hydrocarbons and oxygenates with significantly high faradaic yields.[10, 148] However, as its products upon reaction includes a range of gases and liquids, the design of Cu-based catalytic systems with high production rate and selectivity towards one specific product remains challenging. Regulating the wettability on/near the surface of Cu catalysts has been demonstrated as effective strategies to improve the CO_2RR/CORR performance. Taking the 'plastron effect' used by aquatic arachnids (*e.g.* diving bell spider) as inspiration, direct functionalization of Cu using 1-octadecanethiol to form a hydrophobic alkanethiol overlayer on Cu surface (**Figure 13a**) resulted in suppressed HER and dramatically enhanced Faradaic efficiency for CH_4, C_2H_4 and C_2H_5OH compared to pristine hydrophilic Cu electrode (**Figure 13b**).[149] However, this method also presented a drawback, *i.e.*, decreased current density (**Figure 13c**), which was ascribed to the blocked electrochemically active surface area by the hydrophobic overlayer.[150-152] By comparing the underwater wetting behavior near the hydrophobic Cu surface with that near the hydrophilic surface, it was proposed that the electrolyte-solid-gas three-phase boundary for hydrophobic Cu electrode facilitated omnidirectional CO_2 mass transport with improved local CO_2 availability, which greatly increased the surface concentration of Cu-CO* as a key intermediate for subsequent CH_4 formation and C-C coupling (**Figure 13d**). A fairly stable formation of C_{1-3} products was achieved for at least 5 h.

To circumvent the catalytic site-blocking issue, hydrophobicity can also be induced to the underlayer/substrate or the adjacent catalytically inert solid additive. For instance, a PTFE-treated carbon black microporous underlayer loaded with Cu catalyst gave rise to a 52.7% Faradaic efficiency for C_2H_4 production, which corresponded to ~20 times increment compared to a less hydrophobic 5%-PTFE treated carbon paper substrate (**Figure 13e,f**).[153] Notably, its geometric current density for C_2H_4 was also higher than other substrates with 5-25% PTFE treatment (**Figure 13e**). This configuration favored the formation of three-phase interface without blocking the catalytic sites on Cu surface (**Figure 13g**).[153, 154] Another configuration was demonstrated by mixing Cu catalysts with PTFE particles (Cu/C/PTFE) to create a hydrophobic microenvironment with solid–liquid–gas interfaces (**Figure 13h**). This Cu/C/PTFE electrode showed higher current densities across all the examined potentials (**Figure 13i**) and higher total Faradaic efficiency for CO_2RR as well as C_{2+} Faradaic efficiency than those for Cu/C electrode without PTFE. The blended PTFE particles effectively sustain the hydrophobicity of the electrode (*i.e.* three-phase interface) during electrochemical CO_2RR (**Figure 13j**). The issue about electrolyte flooding under high-rate operation was also addressed using a bioinspired copper catalyst on a gas diffusion layer that mimicked the unique hierarchical structuring of Setaria's hydrophobic leaves.[155] Specifically, outstanding stability at 300 mA cm^{-2} over 45 h was achieved in a flow reactor, largely outperforming its wettable copper counterparts. Lastly, a very straightforward strategy was demonstrated by simply placing Cu catalysts in close proximity to a CO_2 plastron layer trapped by superhydrophobic silicon in electrolyte.[156] This configuration turned out to effective for reducing the Faradaic efficiency for HER and enhancing the formation of C_{2+} products.

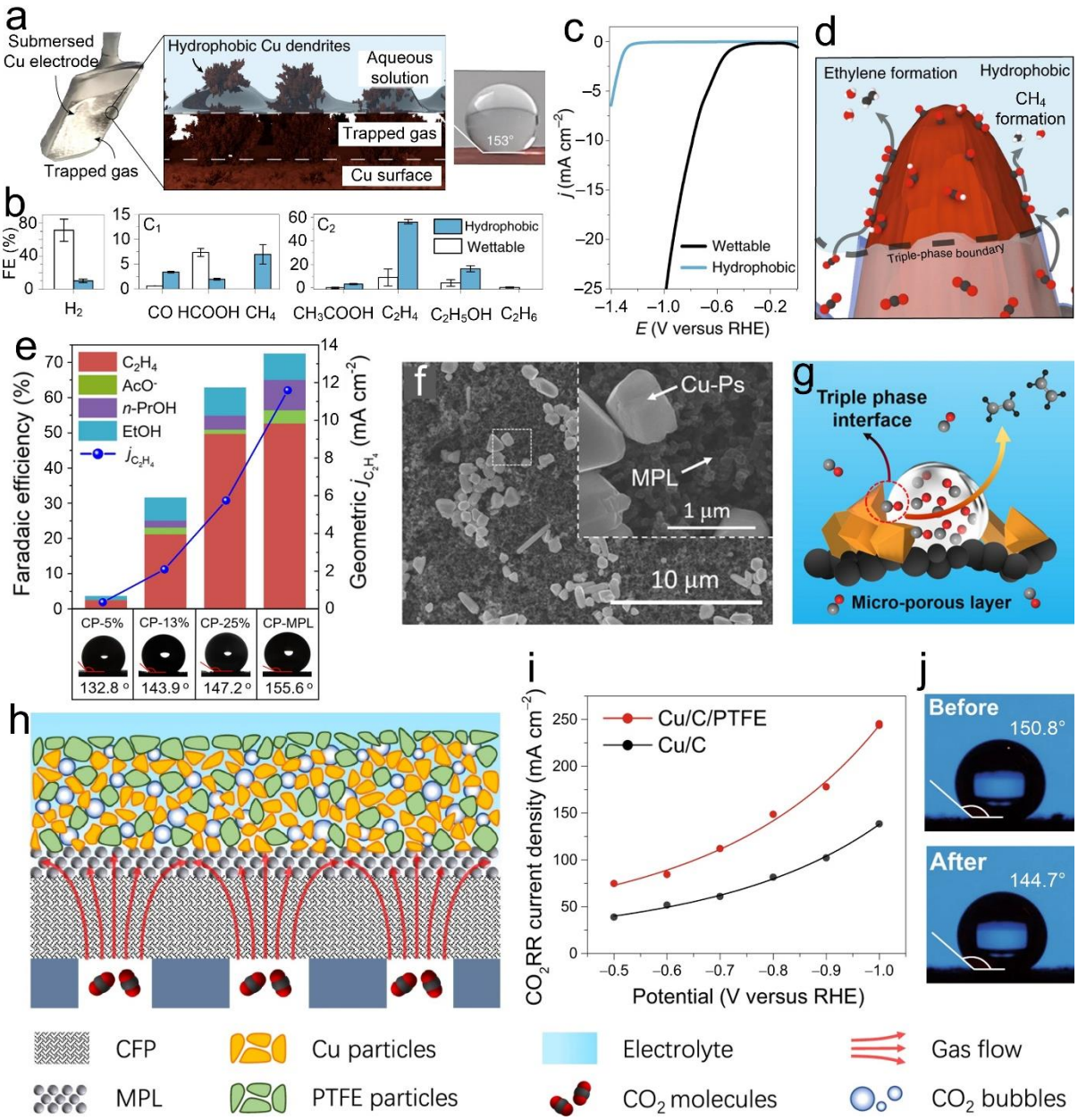

Figure 13. (a) A hydrophobic dendritic Cu electrode for CO_2RRand its water contact angle measurement. (b) Product formation Faradaic efficiencies for the hydrophobic versus wettable electrode. (c) Polarization curves for the wettable and hydrophobic electrodes. (d) The proposed role of hydrophobicity in promoting CO_2RR over proton reduction. Reproduced with permission.[149] Copyright 2019, Springer Nature. (e) Faradaic efficiency and geometric current density for CORR over Cu particles loaded on four types of carbon papers. Bottom pictures show water contact angles on the corresponding carbon papers. (f) SEM images of Cu particles/carbon paper-microporous layer electrode. (g) Schematic illustration for CORR on Cu catalysts assisted by the hydrophobic microporous layer to improve the CO diffusion. Reproduced with permission.[153] Copyright 2020, Wiley-VCH. (h) Hydrophobic microenvironment with solid–liquid–gas interfaces constructed in a gas diffusion electrode cell by dispersing PTFE nanoparticles inside the catalyst layer. (i) Partial current densities for CO_2RR on the Cu/C and Cu/C/PTFE electrodes. (j) Photographs of contact angle measurements on the Cu/C/PTFE electrode before and after CO_2 electrolysis. Reproduced with permission.[157] Copyright 2021, Springer Nature.

Last but not the least, due to the produced alcohols with low surface tension upon CO_2RR/CORR, *i.e.*, 22.5 mN m^{-1} for methanol,[158, 159] 21.8 mN m^{-1} for ethanol,[160, 161] and 23.3 mN m^{-1} for propanol at 25°C,[162-164] the surface tension of initial aqueous electrolyte (72.0 mN m^{-1} at 25°C) with gradually accumulated products will keep decreasing over time. For example, aqueous solution of 10 wt.% methanol, ethanol or 1-propanol have a surface tension of 56.2, 47.5 and 34.3 mN m^{-1} at 25°C, respectively.[165] Consequently, the electrode will eventually be wetted so that the pores in the catalyst layer will be flooded by the electrolyte and the three-phase interface will disappear. This problem can be potentially addressed by fabricating oleophobic/omniphobic electrodes that repel low surface tension liquids (<25 mN m^{-1}) and/or designing novel systems that efficiently remove alcohols and other CO_2RR/CORR products from the electrolyte.

4.5 Photoelectrochemical gas-involving reactions

Photoelectrochemical gas-involving reactions include both GERs and GCRs. Therefore, some of the wettability-related design principles for photoelectrodes are similar to their counterparts for electrolysis. Taking advantage of its high transparency, the aforementioned superaerophobic hydrogel (**Figure 7d** in Section 4.1) was added as an overlayer on Pt nanoparticles-loaded p-type Si photocathode for HER.[35] Under front-side (electrode-electrolyte side) light illumination, there was a substantial increase in the photocurrent density across all the examined potentials after deposition of the porous hydrogel. The chronoamperograms measured at –0.9 V vs. RHE also confirmed that the hydrogel overlayer led to improved stability of the Si photocathode. In addition to deposition of a catalytically inert overlayer on photoelectrodes, integration of superaerophobic/superhydrophilic co-catalysts onto photoelectrodes can potentially contribute to not only rapid bubble release but also suppressed electron-hole recombination and improved water oxidation kinetics. Modification of $BiVO_4$ photoanode using both superhydrophilic Graphdiyne and CoAl layered double hydroxide

catalyst facilitated charge separation and electrode/electrolyte interface charge transfer during photoelectrochemical OER, resulting in enhanced incident photo-to-current conversion efficiency and half-cell solar energy conversion efficiency.[166] However, it is worth noting that a hydrophobic overlayer can also improve the performance of a photoelectrode for gas-evolving reaction. By investigating the TiO_2 nanotube photoanodes modified with 1H,1H,2H,2H-Perfluorooctyl trichlorosilane (PFTS), n-octadecyltrichlorosilane (OTS), 3-aminopropyltriethoxysilane (APTS), polymerized 2-(methacryloyloxy)ethyltrimethylammonium chloride (PMETAC) (denoted as PTFS-TiO_2, OTS-TiO_2, APTS-TiO_2 and PMETAC-g-TiO_2, respectively) ranging from hydrophilic to hydrophobic surfaces (**Figure 14a**), it was discovered that hydrophobic OTS-TiO_2 and PTFS-TiO_2 photoanodes demonstrated higher photocurrent densities and lower onset potentials than hydrophilic ones (**Figure 14b**).[167] The authors proposed that the modification with monolayers was beneficial to the separation and transport of photoinduced electrons and holes. Additionally, based on the theory of electric double layer, due to the coated hydrophobic monolayers with low surface energy on the surface, there are more particles with negative charge (−OH, OH^-) on the inner dense layer. Consequently, the photogenerated holes migrated faster to the interface, which was beneficial to the OER.

Capillary effects have also been utilized to improve photoelectrochemical performance. Firstly, regarding the bubble release behavior, theoretical model and experimental result using TiO_2 nanorod arrays confirmed that morphology-dependent capillarity led to the formation of a liquid layer between the photoelectrode surface and the adhere bubble, thus significantly alleviating the blockage of active sites at the bubble base.[168] Secondly, with respect to the morphological and structural tuning effect, once applying low surface tension ethanol (~22 mN m^{-1}) to high surface energy (1.36 J m^{-2}) metal oxide FeO_x nanoparticulate networks, capillary forces acted between the nanoparticles at the liquid-air interface in the subsequent drying

process (**Figure 14c**). When the capillary forces are larger than the inter-particle cohesion forces, it will result in restructuring of the nanoparticle network (**Figure 14d**). Characterizations showed that the capillary-force-induced self-assembly improved the crystallinity, promoted preferential orientation of the hematite along the [110] direction upon calcination, and thereby enhanced the electrical conductivity of the material, which led to a 12-fold enhancement of photocurrent density at 1.23 V vs. RHE for OER.[169]

For a photoelectrochemical GCR, a hydrophobic/aerophilic photoelectrode is preferential. Regarding photoelectrochemical NRR, a hydrophobic photoelectrode with underwater Wenzel-Cassie coexistent state was fabricated by coating Au nanoparticles and hydrophobic PTFE porous framework on Ti-passivated Si photocathode, denoted as Au-PTFE/TS.[170] It had a liquid contact angle of ~125° and a gas-bubble contact angle of ~88° (**Figure 14e**). The hydrophobicity-induced electrolyte/N_2/Au interface resulted in the close proximity of active protons and N_2 molecules to the Au catalyst on the surface of PTFE framework, which facilitated the intermolecular interactions for hydrogenating N_2 and overcame the rate-determining step of N_2-to-NH_3 fixation (**Figure 14f**). Therefore, after incorporation of the hydrophobic PTFE porous framework, both the yield rate and the Faradic efficiency for NH_3 were remarkably increased on Au-PTFE/TS by ~1.5 and ~4 times, respectively.

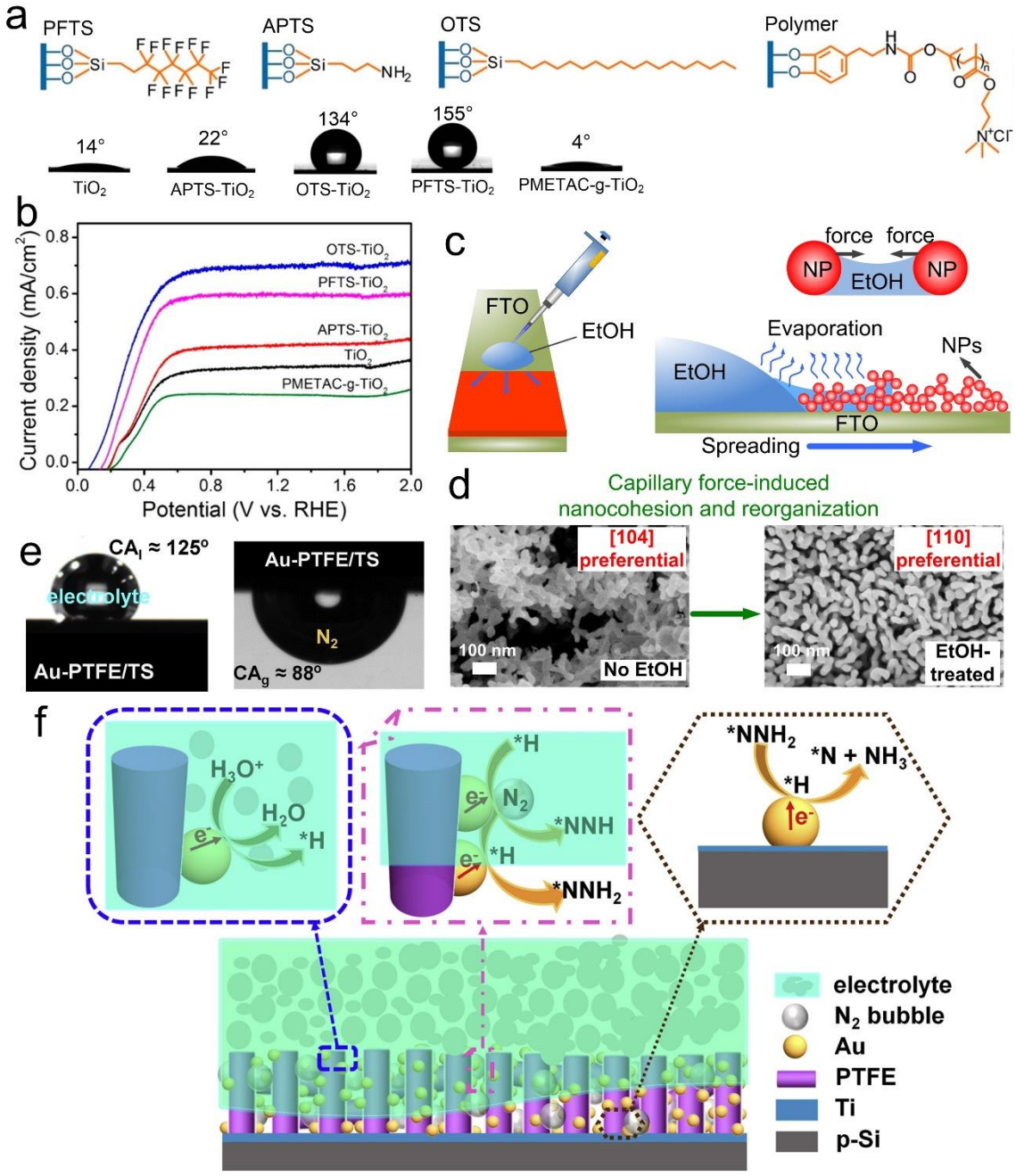

Figure 14. (a) Schematic illustration of molecular monolayer modification of TiO_2 with different chemicals and corresponding contact angle measurements. (b) Photocurrent densities of TiO_2 photoelectrodes before and after chemical modification with different modifiers under illumination. Reproduced with permission.[167] Copyright 2020, American Chemical Society. (c) Schematic diagram of the capillary force-induced re-structuring of Fe_2O_3 photoanodes. (d) SEM images showing corresponding changes in the Fe_2O_3 photoanodes. Reproduced with permission.[169] Copyright 2018, Elsevier Inc. (e) The droplet shape of the electrolyte and the shape of underwater N_2 bubble on the surface of Au-PTFE/TS photocathode. (f) Scheme of NRR enhancement by introducing the aerophilic hierarchical structure on Au-PTFE/TS photocathode. Reproduced with permission.[170] Copyright 2018, Elsevier Inc.

Light harvesting is an additional key parameter for photoelectrocatalysis to enhance the solar-to-fuel conversion efficiency, which has also been inspired by nature. One strategy towards improved light trapping is to develop antireflective surfaces. Intricate surface architectures with tapered shapes (*e.g.* cones, pillars and columns) can minimize the light reflection based on a subwavelength diffraction grating mechanism, which have been found in moth eyes and butterfly wings (**Figure 15a**).[171, 172] For example, patterning mesoporous TiO_2 layers with conical shaped moth-eye structures (**Figure 15b**) led to significantly enhanced optical absorption compared to flat TiO_2 surface (**Figure 15c**).[173] Moreover, leaves as the light harvester for green plants have evolved to maximize their photon harvesting capabilities. Accordingly, ZnO-based fern-like microleaves exhibited superior light absorption independent of incident light angle to ZnO nanorods and nanowires (**Figure 15d**).[174] Artificial N-doped ZnO leaf demonstrated increased light absorbance within the visible light range by up to 131% and redshift of bandgap absorption edge compared to the bulk counterpart (**Figure 15e,f**).[175] Another feasible biomimetic strategy to enhance light harvesting is based on phototropism. This phenomenon occurs when plants such as sunflowers self-orient to face the sun throughout the day (**Figure 15g**). Phototropism enabled the tips of the sunflower-like omnidirectional tracker fibrils always received the maximum photonic power density at oblique illumination angles, which achieved up to a 400% solar energy-harvesting enhancement over non-tropistic materials.[176] Similarly, a 'bionic sunflower' based on a light-responsive hydrogel was reported.[177] When it was used for photo-driven ORR, a ~3 times higher H_2O_2 yield rate was achieved than the same system without phototropism.

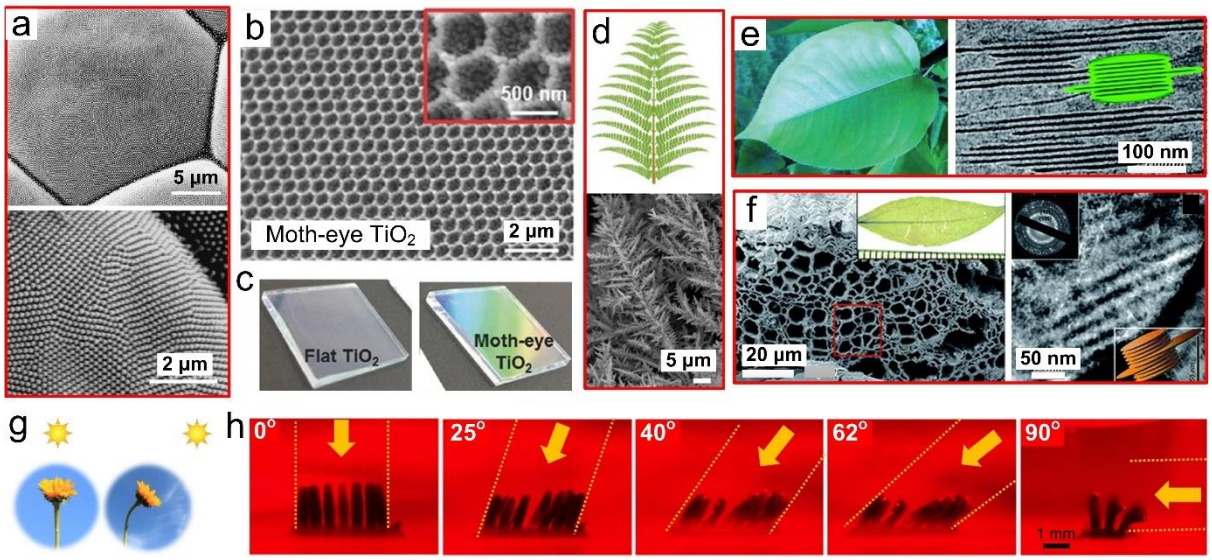

Figure 15. (a) SEM images of corneal nipple arrays in the peacock (*Inachis io*), a nymphalid butterfly. Reproduced with permission.[171] Copyright 2005, The Royal Society. (b) SEM image of moth-eye patterned TiO_2 layer. (c) Optical images of the glass substrates with flat TiO_2 and moth-eye TiO_2. Reproduced with permission.[173] Copyright 2016, Wiley-VCH. (d) Schematic representation of microfern leaf and SEM image of ZnO-based fern-like microleaves. Reproduced with permission.[174] Copyright 2019, Elsevier Inc. (e) Optical and TEM images of original *Cinnamomum camphora* leaf. (f) SEM and TEM images of artificial N-doped ZnO leaf. Reproduced with permission.[175] Copyright 2009, The Royal Society of Chemistry. (g) Phototropism of sunflowers. (h) Side-view photos of biomimetic omnidirectional tracker tracking various angles of incidence light (0–90°). Reproduced with permission.[176] Copyright 2019, Springer Nature.

5. Conclusion and outlook

Wettability-regulation during the design of (photo)electrodes is an effective strategy towards improving (photo)electrocatalytic performance. In this review, we have summarized the fundamentals of a range of wetting states and corresponding strategies towards practical applications in various (photo)electrochemical reactions. In addition to (photo)electrocatalysis, wettability-regulation can also contribute to improved Fischer-Tropsch process[178] and biologically relevant catalysis.[179] However, great challenges remain as this is an emerging field lacking in comprehensive mechanistic studies and systematic design principles. Applying the principles of surface wettability to catalytic systems is rather complicated owing to diverse surface physicochemical properties and specific operational conditions. Future efforts can be made on the basis of the following aspects:

First, with respect to GERs, superhydrophilic/superaerophobic (photo)electrode surfaces are preferable for bubble detachment. Besides the intrinsic properties of the catalytic materials, design of (photo)electrodes with minimal bubble-to-surface contact area, such as nanoneedle arrays, can significantly decrease the adhesion force of bubbles, thus enabling rapid bubble release.

Second, superhydrophobic/superaerophilic (photo)electrodes with underwater Wenzel-Cassie coexistent state are favorable for GCRs. However, the durability of underwater superaerophilicity as a common issue is much less investigated.[180] More specifically, these (photo)electrodes should demonstrate immersion-stable superaerophilicity, maintaining a durable plastron layer of gas reactant, thus enabling a long-term three-phase for reactions. Regarding some CO_2RR systems, accumulated alcohol products are produced in the electrolyte upon CO_2RR. This leads to effect of decreased electrolyte surface tension. As a result, the development of robust superoleophobic/superomniphobic electrode surfaces is necessary.

Third, novel structural design of 3D electrodes or functional overlayer/underlayer for electrodes can be tailored to the requirements of GERs and GCRs, respectively. Effective tools for modelling of the bubble transport and gas diffusion behaviors inside/near the electrodes are necessary to achieve optimal design parameters. The use of gas-permeable membranes could be also be adapted to fabricate novel electrode architectures for gas-involving reactions.[181, 182]

Fourth, industrially viable fabrication techniques are highly desirable for scale-up of the superwetting electrodes and photoelectrodes. A roll-to-roll technique is promising to addressing this issue.[5] Amongst various deposition methods, spray coating (**Figure 16a**) and screen printing (**Figure 16b**) are compatible with this technique. Both traditional wet spray coating and screen-printing methods have been used for electrode and photoelectrode fabrication.[183-188] While introducing superwetting properties to the (photo)electrodes, additional functionalization step or physically adding superwetting materials is generally

indispensable (*vide supra*). However, one-step fabrication of superhydrophobic catalytic layers was also feasible using flame spray pyrolysis based on on-the-fly hydrophobization (**Figure 16c**).[189] Notably, Flame spray pyrolysis as an aerosol deposition method is highly scalable for facile and fast fabrication of various nanostructured (photo)electrodes.[169, 190-192] A production rate of a few kilograms per hour has been achieved using lab-scale burners with tunable specific surface area and catalytic activity for the produced nanomaterials.[193, 194] Furthermore, a post-synthetic gas-phase fluorosilanization method was applicable for modification of large-size (photo)electrodes towards superoleophobicity (**Figure 16d**).[195]

In recent years, emerging macroscopic-scale model fabrication techniques such as 3D printing (*i.e.* additive manufacturing) has been extended towards materials such as metals and thus metal oxides.[196] The maturation of additive manufacturing will likely lead to developments in printable materials, including (photo)electrodes. The integration of 3D-printing with micro-metrically accurate CNC milling and nano-metrically accurate laser ablation can potentially impart hierarchically structured model designs.[197, 198] The use of precise laser ablation may also enable surface chemistry patterning and therefore direct wettability and plastron control. With the rapid advancements and widespread availability of these manufacturing methods (3D-priting, CNC-milling, and laser ablation), we envision that they will eventually be implemented towards developing highly precise and model architectures to manipulate bubble transport, gas diffusion and light harvesting behaviors.[199]

The advancement of the field will likely be guided by both model and stochastic fabrication methods, with effective usage determined by cost-energy storage parity ratios ($/W). Regardless of the precision and scalability involved, the efficient control and use of (super)wettability for the enhancement of electrocatalytic efficiency (selectivity, limiting current density, etc.) would likely spur future electrode developments.

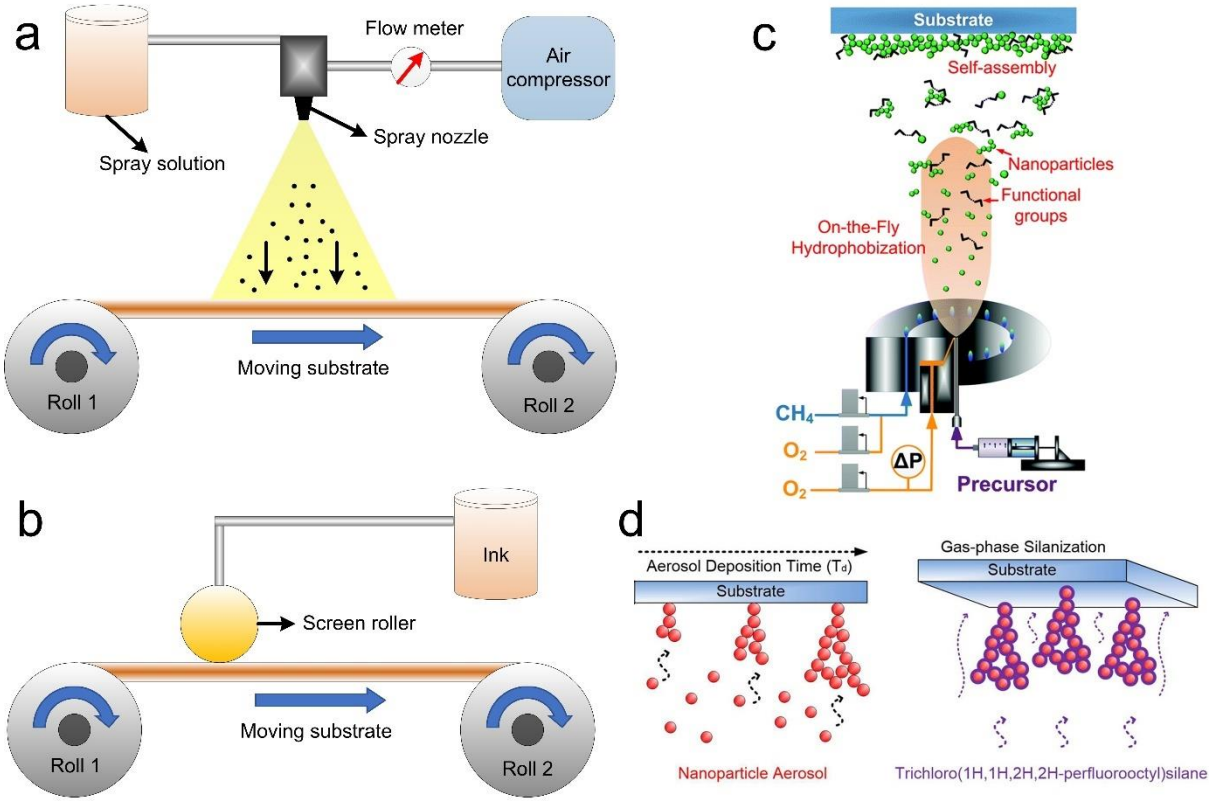

Figure 16. Schematic illustrations of (a) spray roll-to-roll coating technique and (b) rotary screen-printing technique. Reproduced with permission.[5] Copyright 2019, Elsevier Inc. (c) Schematic diagram of one-step synthesis of superhydrophobic nano-layers via flame spray pyrolysis. Reproduced with permission.[189] Copyright 2016, The Royal Society of Chemistry. (d) Schematic description of fluorosilanization process by an atmospheric pressure chemical vapor deposition (APCVD) method to achieve superoleophobicity. Reproduced with permission.[195] Copyright 2016, American Chemical Society

Acknowledgements

This work is supported by the eCO_2EP programme funded by the Singapore National Research Foundation under its Campus for Research Excellence and Technological Enterprise (CREATE) programme through the Cambridge Centre for Advanced Research and Education in Singapore (CARES) and the Berkeley Educational Alliance for Research in Singapore (BEARS). W.S.Y.W and D.V. acknowledges the European Union's Horizon 2020 research and innovation program LubISS No. 722497 and the ERC Advanced Grant (883631 DynaMo).

Chem. Soc. Rev., 2021,50, 10674-10699, https://doi.org/10.1039/D1CS00258A

References

1. N. S. Lewis and D. G. Nocera, *Proc. Natl Acad. Sci. USA*, 2006, **103**, 15729-15735.
2. J. A. Turner, *Science*, 2004, **305**, 972-974.
3. W. Xu, Z. Lu, X. Sun, L. Jiang and X. Duan, *Acc. Chem. Res.*, 2018, **51**, 1590-1598.
4. J. Song, C. Wei, Z.-F. Huang, C. Liu, L. Zeng, X. Wang and Z. J. Xu, *Chem. Soc. Rev.*, 2020, **49**, 2196-2214.
5. G. Liu, Y. Sheng, J. W. Ager, M. Kraft and R. Xu, *EnergyChem*, 2019, **1**, 100014.
6. J. Zhu, L. Hu, P. Zhao, L. Y. S. Lee and K.-Y. Wong, *Chem. Rev.*, 2020, **120**, 851-918.
7. C. Guo, J. Ran, A. Vasileff and S.-Z. Qiao, *Energy Environ. Sci.*, 2018, **11**, 45-56.
8. A. Kulkarni, S. Siahrostami, A. Patel and J. K. Nørskov, *Chem. Rev.*, 2018, **118**, 2302-2312.
9. M. Shao, Q. Chang, J.-P. Dodelet and R. Chenitz, *Chem. Rev.*, 2016, **116**, 3594-3657.
10. S. Nitopi, E. Bertheussen, S. B. Scott, X. Liu, A. K. Engstfeld, S. Horch, B. Seger, I. E. L. Stephens, K. Chan, C. Hahn, J. K. Norskov, T. F. Jaramillo and I. Chorkendorff, *Chem. Rev.*, 2019, **119**, 7610-7672.
11. G. Liu, T. Tran-Phu, H. Chen and A. Tricoli, *Adv. Sustainable Syst.*, 2018, **2**, 1800028.
12. H. Vogt, *Electrochim. Acta*, 2017, **235**, 495-499.
13. W. Lubitz, M. Chrysina and N. Cox, *Photosynth. Res.*, 2019, **142**, 105-125.
14. B. K. Burgess and D. J. Lowe, *Chem. Rev.*, 1996, **96**, 2983-3012.
15. M. Liu, S. Wang and L. Jiang, *Nat. Rev. Mater.*, 2017, **2**, 17036.
16. G. B. Darband, M. Aliofkhazraei and S. Shanmugam, *Renew. Sustain. Energy Rev.*, 2019, **114**, 109300.
17. X. Zhao, H. Ren and L. Luo, *Langmuir*, 2019, **35**, 5392-5408.
18. M. Wang, X. Yu, Z. Wang, X. Gong, Z. Guo and L. Dai, *J. Mater. Chem. A*, 2017, **5**, 9488-9513.
19. Z. Lu, Y. Li, X. Lei, J. Liu and X. Sun, *Mater. Horiz.*, 2015, **2**, 294-298.
20. Y. Wang, Y. Zou, L. Tao, Y. Wang, G. Huang, S. Du and S. Wang, *Nano Res.*, 2019, **12**, 2055-2066.
21. S. K. Mazloomi and N. Sulaiman, *Renew. Sustain. Energy Rev.*, 2012, **16**, 4257-4263.
22. M. S. Faber, R. Dziedzic, M. A. Lukowski, N. S. Kaiser, Q. Ding and S. Jin, *J. Am. Chem. Soc.*, 2014, **136**, 10053-10061.
23. N. Gao, F. Geyer, D. W. Pilat, S. Wooh, D. Vollmer, H.-J. Butt and R. Berger, *Nature Phys.*, 2017, **14**, 191.
24. in *Surface and Interfacial Forces*, 2010, DOI: https://doi.org/10.1002/9783527629411.ch8, pp. 219-250.
25. E. Dussan V., *J. Fluid Mech.*, 1985, **151**, 1-20.
26. J. Zhang, X. Sheng, X. Cheng, L. Chen, J. Jin and X. Feng, *Nanoscale*, 2017, **9**, 87-90.
27. C. Yu, P. Zhang, J. Wang and L. Jiang, *Adv. Mater.*, 2017, **29**, 1703053.
28. K. D. Danov, R. D. Stanimirova, P. A. Kralchevsky, K. G. Marinova, S. D. Stoyanov, T. B. J. Blijdenstein, A. R. Cox and E. G. Pelan, *Advances in Colloid and Interface Science*, 2016, **233**, 223-239.
29. P. Wang, T. Hayashi, Q. a. Meng, Q. Wang, H. Liu, K. Hashimoto and L. Jiang, *Small*, 2017, **13**, 1601250.
30. T. Kou, S. Wang, R. Shi, T. Zhang, S. Chiovoloni, J. Q. Lu, W. Chen, M. A. Worsley, B. C. Wood, S. E. Baker, E. B. Duoss, R. Wu, C. Zhu and Y. Li, *Adv. Energy Mater.*, 2020, **10**, 2002955.
31. T. Burdyny, P. J. Graham, Y. Pang, C.-T. Dinh, M. Liu, E. H. Sargent and D. Sinton, *ACS Sustainable Chem. Eng.*, 2017, **5**, 4031-4040.
32. T. Young, *Phil. Trans. R. Soc.*, 1805, **95**, 65-87.
33. Y. Tian, B. Su and L. Jiang, *Adv. Mater.*, 2014, **26**, 6872-6897.
34. B. Su, Y. Tian and L. Jiang, *J. Am. Chem. Soc.*, 2016, **138**, 1727-1748.
35. D. Jeon, J. Park, C. Shin, H. Kim, J.-W. Jang, D. W. Lee and J. Ryu, *Sci. Adv.*, 2020, **6**, eaaz3944.
36. J. T. Korhonen, T. Huhtamäki, O. Ikkala and R. H. A. Ras, *Langmuir*, 2013, **29**, 3858-3863.
37. H. B. Eral, D. J. C. M. 't Mannetje and J. M. Oh, *Colloid Polym. Sci.*, 2013, **291**, 247-260.

38. L. Gao and T. J. McCarthy, *Langmuir*, 2006, **22**, 6234-6237.
39. W. S. Y. Wong, L. Hauer, A. Naga, A. Kaltbeitzel, P. Baumli, R. Berger, M. D'Acunzi, D. Vollmer and H.-J. Butt, *Langmuir*, 2020, **36**, 7236-7245.
40. Y. Yuan and T. R. Lee, in *Surface Science Techniques*, eds. G. Bracco and B. Holst, Springer Berlin Heidelberg, Berlin, Heidelberg, 2013, DOI: 10.1007/978-3-642-34243-1_1, pp. 3-34.
41. C. W. Extrand, *Langmuir*, 2003, **19**, 3793-3796.
42. W. S. Y. Wong and A. Tricoli, *ACS Appl. Mater. Interfaces*, 2018, **10**, 13999-14007.
43. Y. Pomeau and J. Vannimenus, *J. Colloid Interface Sci.*, 1985, **104**, 477-488.
44. J. F. Joanny and P. G. de Gennes, *J. Chem. Phys.*, 1984, **81**, 552-562.
45. B. Andreotti and J. H. Snoeijer, *Annual Review of Fluid Mechanics*, 2019, DOI: 10.1146/annurev-fluid-010719-060147.
46. M. van Gorcum, B. Andreotti, J. H. Snoeijer and S. Karpitschka, *Phys. Rev. Lett.*, 2018, **121**, 208003.
47. J. H. Snoeijer and B. Andreotti, *Annual Review of Fluid Mechanics*, 2013, **45**, 269-292.
48. F. Schellenberger, N. Encinas, D. Vollmer and H.-J. Butt, *Physical review letters*, 2016, **116**, 096101.
49. R. N. Wenzel, *Ind. Eng. Chem. Res.*, 1936, **28**, 988-994.
50. F. Ç. Cebeci, Z. Wu, L. Zhai, R. E. Cohen and M. F. Rubner, *Langmuir*, 2006, **22**, 2856-2862.
51. A. Tricoli, M. Righettoni and S. E. Pratsinis, *Langmuir*, 2009, **25**, 12578-12584.
52. S. Wang, K. Liu, X. Yao and L. Jiang, *Chem. Rev.*, 2015, **115**, 8230-8293.
53. C. Ishino, M. Reyssat, E. Reyssat, K. Okumura and D. Quéré, *EPL*, 2007, **79**, 56005.
54. E. Martines, K. Seunarine, H. Morgan, N. Gadegaard, C. D. W. Wilkinson and M. O. Riehle, *Nano Lett.*, 2005, **5**, 2097-2103.
55. A. Y. Vorobyev and C. Guo, *Opt. Express*, 2010, **18**, 6455-6460.
56. J. Bico, U. Thiele and D. Quéré, *Colloids Surf. A*, 2002, **206**, 41-46.
57. H. Teisala, M. Tuominen, M. Aromaa, M. Stepien, J. M. Makela, J. J. Saarinen, M. Toivakka and J. Kuusipalo, *Langmuir*, 2012, **28**, 3138-3145.
58. M. Nosonovsky and B. Bhushan, *Lotus Versus Rose: Biomimetic Surface Effects*, Springer, Berlin, Germany, 2012.
59. L. Jiang, Y. Zhao and J. Zhai, *Angew. Chem. Int. Ed.*, 2004, **43**, 4338-4341.
60. A. Cassie and S. Baxter, *J. Chem. Soc. Faraday Trans.*, 1944, **40**, 546-551.
61. F. Schellenberger, N. Encinas, v. doris and H.-J. Butt, *How Water Advances on Superhydrophobic Surfaces*, 2016.
62. E. Brillas, A. Serrà and S. Garcia-Segura, *Curr. Opin. Electrochem.*, 2021, **26**, 100660.
63. H. G. Edelmann, C. Neinhuis, M. Jarvis, B. Evans, E. Fischer and W. Barthlott, *Planta*, 1998, **206**, 315-321.
64. K. Koch and W. Barthlott, *Philos. Trans. R. Soc. A*, 2009, **367**, 1487-1509.
65. L. F. Wang and Z. D. Dai, *Biosurface and Biotribology*, 2016, **2**, 70-74.
66. X. Yu, Z. Y. Yu, X. L. Zhang, Y. R. Zheng, Y. Duan, Q. Gao, R. Wu, B. Sun, M. R. Gao, G. Wang and S. H. Yu, *J. Am. Chem. Soc.*, 2019, **141**, 7537-7543.
67. Y. Li, H. Zhang, T. Xu, Z. Lu, X. Wu, P. Wan, X. Sun and L. Jiang, *Adv. Funct. Mater.*, 2015, **25**, 1737-1744.
68. R. Shi, J. Guo, X. Zhang, G. I. N. Waterhouse, Z. Han, Y. Zhao, L. Shang, C. Zhou, L. Jiang and T. Zhang, *Nat. Commun.*, 2020, **11**, 3028.
69. Z. Lu, W. Xu, J. Ma, Y. Li, X. Sun and L. Jiang, *Adv. Mater.*, 2016, **28**, 7155-7161.
70. Q. Xu, W. Zhang, C. Dong, T. S. Sreeprasad and Z. Xia, *J. R. Soc. Interface*, 2016, **13**, 20160300.
71. W. Barthlott, M. Mail, B. Bhushan and K. Koch, *Nano-Micro Letters*, 2017, **9**, 23.
72. W. Barthlott and C. Neinhuis, *Planta*, 1997, **202**, 1-8.
73. F. Geyer, M. D'Acunzi, A. Sharifi-Aghili, A. Saal, N. Gao, A. Kaltbeitzel, T.-F. Sloot, R. Berger, H.-J. Butt and D. Vollmer, *Sci. Adv.*, 2020, **6**, eaaw9727.
74. N. Le Grand, A. Daerr and L. Limat, *J. Fluid Mech.*, 2005, **541**, 293-315.

75. P. G. de Gennes, F. Brochard-Wyart and D. Quere, *Capillarity and Wetting Phenomena: Drops, Bubbles, Pearls, Waves*, 2003.
76. H. Princen, *Colloids Surf.*, 1969, **2**, 1-84.
77. A. Angulo, P. van der Linde, H. Gardeniers, M. Modestino and D. Fernández Rivas, *Joule*, 2020, **4**, 555-579.
78. J. Chen and L. Guo, *Applied Physics Letters*, 2019, **114**, 231604.
79. Y. Li, H. Zhang, T. Xu, Z. Lu, X. Wu, P. Wan, X. Sun and L. Jiang, *Adv. Funct. Mater.*, 2015, **25**, 1737-1744.
80. T. Burdyny, P. J. Graham, Y. Pang, C.-T. Dinh, M. Liu, E. H. Sargent and D. Sinton, *ACS Sustainable Chemistry & Engineering*, 2017, **5**, 4031-4040.
81. N. Le Grand, A. Daerr and L. Limat, *Journal of Fluid Mechanics*, 2005, **541**, 293-315.
82. G. Duhar and C. Colin, *Physics of Fluids*, 2006, **18**, 077101.
83. R. Kumar and N. K. Kuloor, in *Advances in Chemical Engineering*, eds. T. B. Drew, G. R. Cokelet, J. W. Hoopes and T. Vermeulen, Academic Press, 1970, vol. 8, pp. 255-368.
84. A. D. Polyanin and A. V. Manzhirov, *Handbook of Mathematics for Engineers and Scientists*, CRC Press, 2006.
85. S. B. G. M. O'Brien and B. H. A. A. van den Brule, *J. Chem. Soc. Faraday Trans.*, 1991, **87**, 1579-1583.
86. H.-J. Butt, I. V. Roisman, M. Brinkmann, P. Papadopoulos, D. Vollmer and C. Semprebon, *Curr. Opin. Colloid Interface Sci.*, 2014, **19**, 343-354.
87. H.-J. Butt, N. Gao, P. Papadopoulos, W. Steffen, M. Kappl and R. Berger, *Langmuir*, 2017, **33**, 107-116.
88. A. Papra, N. Gadegaard and N. B. Larsen, *Langmuir*, 2001, **17**, 1457-1460.
89. Y. Li, J. Q. Pham, K. P. Johnston and P. F. Green, *Langmuir*, 2007, **23**, 9785-9793.
90. C. W. Extrand and Y. Kumagai, *J. Colloid Interface Sci.*, 1995, **170**, 515-521.
91. C. Antonini, F. J. Carmona, E. Pierce, M. Marengo and A. Amirfazli, *Langmuir*, 2009, **25**, 6143-6154.
92. A. I. ElSherbini and A. M. Jacobi, *Journal of Colloid and Interface Science*, 2006, **299**, 841-849.
93. N. Gao, F. Geyer, D. W. Pilat, S. Wooh, D. Vollmer, H.-J. Butt and R. Berger, *Nature Phys.*, 2018, **14**, 191-196.
94. W. S. Y. Wong, T. P. Corrales, A. Naga, P. Baumli, A. Kaltbeitzel, M. Kappl, P. Papadopoulos, D. Vollmer and H.-J. Butt, *ACS Nano*, 2020, **14**, 3836-3846.
95. S. Chen, B. Zhang, X. Gao, Z. Liu and X. Zhang, *Langmuir*, 2017, **33**, 2472-2476.
96. C. Shi, X. Cui, X. Zhang, P. Tchoukov, Q. Liu, N. Encinas, M. Paven, F. Geyer, D. Vollmer, Z. Xu, H.-J. Butt and H. Zeng, *Langmuir*, 2015, **31**, 7317-7327.
97. B. Liu, R. Manica, Q. Liu, E. Klaseboer, Z. Xu and G. Xie, *Phys. Rev. Lett.*, 2019, **122**, 194501.
98. D. Y. C. Chan, E. Klaseboer and R. Manica, *Soft Matter*, 2011, **7**, 2235-2264.
99. J. Lv, Z. Gong, Z. He, J. Yang, Y. Chen, C. Tang, Y. Liu, M. Fan and W.-M. Lau, *J. Mater. Chem. A*, 2017, **5**, 12435-12444.
100. Z. Lu, L. Zhang, R. Iwata, E. N. Wang and J. C. Grossman, *Langmuir*, 2020, **36**, 15112-15118.
101. Y. Liu, C. Jin, Y. Liu, K. H. Ruiz, H. Ren, Y. Fan, H. S. White and Q. Chen, *ACS Sensors*, 2020, DOI: 10.1021/acssensors.0c00913.
102. Q. Wang, K. Cui, J. Li, Y. Wu, Y. Yang, X. Zhou, G. Ma, Z. Yang, Z. Lei and S. Ren, *Nanoscale*, 2020, **12**, 16208-16214.
103. B. Liu, C. Wu, G. Chen, W. Chen, L. Peng, Y. Yao, Z. Wei, H. Zhu, T. Han, D. Tang and M. Zhou, *J. Power Sources*, 2019, **429**, 46-54.
104. N. Han, K. R. Yang, Z. Lu, Y. Li, W. Xu, T. Gao, Z. Cai, Y. Zhang, V. S. Batista, W. Liu and X. Sun, *Nat. Commun.*, 2018, **9**, 924.
105. Z. Lu, W. Zhu, X. Yu, H. Zhang, Y. Li, X. Sun, X. Wang, H. Wang, J. Wang, J. Luo, X. Lei and L. Jiang, *Adv. Mater.*, 2014, **26**, 2683-2687.

106. L. Shang, Y. Zhao, X.-Y. Kong, R. Shi, G. I. N. Waterhouse, L. Wen and T. Zhang, *Nano Energy*, 2020, **78**, 105375.
107. K. Akbar, S. Hussain, L. Truong, S. B. Roy, J. H. Jeon, S.-K. Jerng, M. Kim, Y. Yi, J. Jung and S.-H. Chun, *ACS Appl. Mater. Interfaces*, 2017, **9**, 43674-43680.
108. Q. Zhang, P. Li, D. Zhou, Z. Chang, Y. Kuang and X. Sun, *Small*, 2017, **13**, 1701648.
109. H. Zhang, Z. Feng, L. Wang, D. Li and P. Xing, *Nanotechnology*, 2020, **31**, 365701.
110. M. Das, N. Jena, T. Purkait, N. Kamboj, A. De Sarkar and R. S. Dey, *J. Mater. Chem. A*, 2019, **7**, 23989-23999.
111. H. Sun, X. Xu, Z. Yan, X. Chen, L. Jiao, F. Cheng and J. Chen, *J. Mater. Chem. A*, 2018, **6**, 22062-22069.
112. W.-B. Jung, G.-T. Yun, Y. Kim, M. Kim and H.-T. Jung, *ACS Appl. Mater. Interfaces*, 2019, **11**, 7546-7552.
113. C. Yu, M. Cao, Z. Dong, K. Li, C. Yu, J. Wang and L. Jiang, *Adv. Funct. Mater.*, 2016, **26**, 6830-6835.
114. J. Li, R. Guttinger, R. More, F. Song, W. Wan and G. R. Patzke, *Chem. Soc. Rev.*, 2017, **46**, 6124-6147.
115. A. Nayak, S. Roy, B. D. Sherman, L. Alibabaei, A. M. Lapides, M. K. Brennaman, K.-R. Wee and T. J. Meyer, *ACS Appl. Mater. Interfaces*, 2016, **8**, 3853-3860.
116. X. Liu, S. Inagaki and J. Gong, *Angew. Chem., Int. Ed.*, 2016, **55**, 14924-14950.
117. M. K. Brennaman, R. J. Dillon, L. Alibabaei, M. K. Gish, C. J. Dares, D. L. Ashford, R. L. House, G. J. Meyer, J. M. Papanikolas and T. J. Meyer, *J. Am. Chem. Soc.*, 2016, **138**, 13085-13102.
118. K. E. deKrafft, C. Wang, Z. Xie, X. Su, B. J. Hinds and W. Lin, *ACS Appl. Mater. Interfaces*, 2012, **4**, 608-613.
119. L. Tong, M. Göthelid and L. Sun, *Chem. Commun.*, 2012, **48**, 10025-10027.
120. J. D. Blakemore, A. Gupta, J. J. Warren, B. S. Brunschwig and H. B. Gray, *J. Am. Chem. Soc.*, 2013, **135**, 18288-18291.
121. N. Morlanés, K. Takanabe and V. Rodionov, *ACS Catal.*, 2016, **6**, 3092-3095.
122. E. L. Demeter, S. L. Hilburg, N. R. Washburn, T. J. Collins and J. R. Kitchin, *J. Am. Chem. Soc.*, 2014, **136**, 5603-5606.
123. J. Masud, P.-C. Ioannou, N. Levesanos, P. Kyritsis and M. Nath, *ChemSusChem*, 2016, **9**, 3128-3132.
124. B.-T. Chen, N. Morlanés, E. Adogla, K. Takanabe and V. O. Rodionov, *ACS Catal.*, 2016, **6**, 4647-4652.
125. S. Zhan, B. Zhang, L. Sun and M. S. G. Ahlquist, *ACS Catal.*, 2020, **10**, 13364-13370.
126. K. Dastafkan, Y. Li, Y. Zeng, L. Han and C. Zhao, *J. Mater. Chem. A*, 2019, **7**, 15252-15261.
127. Y. Li and C. Zhao, *ACS Catal.*, 2017, **7**, 2535-2541.
128. Y. Wang, Y. Li, L. Ding, X. Xu, Z. Chen, C. Li and J. Ding, *Chem. Commun.*, 2019, **55**, 4503-4506.
129. J. He, B. Hu and Y. Zhao, *Adv. Funct. Mater.*, 2016, **26**, 5998-6004.
130. J. Liu, H. Yuan, Z. Wang, J. Li, M. Yang, L. Cao, G. Liu, D. Qian and Z. Lu, *Chem. Commun.*, 2019, **55**, 10860-10863.
131. K. Dastafkan, Q. Meyer, X. Chen and C. Zhao, *Small*, 2020, **16**, 2002412.
132. Y. J. Kim, A. Lim, J. M. Kim, D. Lim, K. H. Chae, E. N. Cho, H. J. Han, K. U. Jeon, M. Kim, G. H. Lee, G. R. Lee, H. S. Ahn, H. S. Park, H. Kim, J. Y. Kim and Y. S. Jung, *Nat. Commun.*, 2020, **11**, 4921.
133. J. Li, Y. Zhu, W. Chen, Z. Lu, J. Xu, A. Pei, Y. Peng, X. Zheng, Z. Zhang, S. Chu and Y. Cui, *Joule*, 2019, **3**, 557-569.
134. W. Xu, Z. Lu, P. Wan, Y. Kuang and X. Sun, *Small*, 2016, **12**, 2492-2498.
135. X. Shan, J. Liu, H. Mu, Y. Xiao, B. Mei, W. Liu, G. Lin, Z. Jiang, L. Wen and L. Jiang, *Angew. Chem. Int. Ed.*, 2020, **59**, 1659-1665.
136. H. Li, S. Chen, Y. Zhang, Q. Zhang, X. Jia, Q. Zhang, L. Gu, X. Sun, L. Song and X. Wang, *Nat. Commun.*, 2018, **9**, 2452.
137. J. Hao, W. Yang, Z. Huang and C. Zhang, *Adv. Mater. Interfaces*, 2016, **3**, 1600236.

138. Y. Tian, Z. Lin, J. Yu, S. Zhao, Q. Liu, J. Liu, R. Chen, Y. Qi, H. Zhang, R. Li, J. Li and J. Wang, *ACS Sustainable Chem. Eng.*, 2019, **7**, 14639-14646.
139. X.-W. Lv, Y. Liu, W. Tian, L. Gao and Z.-Y. Yuan, *J. Energy Chem.*, 2020, **50**, 324-331.
140. R. Xu, R. Wu, Y. Shi, J. Zhang and B. Zhang, *Nano Energy*, 2016, **24**, 103-110.
141. L. Wang, X. Huang, S. Jiang, M. Li, K. Zhang, Y. Yan, H. Zhang and J. M. Xue, *ACS Appl. Mater. Interfaces*, 2017, **9**, 40281-40289.
142. Z.-L. Wang, D. Xu, J.-J. Xu and X.-B. Zhang, *Chem. Soc. Rev.*, 2014, **43**, 7746-7786.
143. W. Tian, H. Li, B. Qin, Y. Xu, Y. Hao, Y. Li, G. Zhang, J. Liu, X. Sun and X. Duan, *J. Mater. Chem. A*, 2017, **5**, 7103-7110.
144. W. Xu, Z. Lu, T. Zhang, Y. Zhong, Y. Wu, G. Zhang, J. Liu, H. Wang and X. Sun, *Energy Storage Mater.*, 2019, **17**, 358-365.
145. Y. Li, H. Zhang, N. Han, Y. Kuang, J. Liu, W. Liu, H. Duan and X. Sun, *Nano Res.*, 2019, **12**, 177-182.
146. K. Dong, J. Liang, Y. Wang, Z. Xu, Q. Liu, Y. Luo, T. Li, L. Li, X. Shi, A. M. Asiri, Q. Li, D. Ma and X. Sun, *Angew. Chem. Int. Ed.*, 2021, DOI: https://doi.org/10.1002/anie.202101880.
147. J. Li, G. Chen, Y. Zhu, Z. Liang, A. Pei, C.-L. Wu, H. Wang, H. R. Lee, K. Liu, S. Chu and Y. Cui, *Nat. Catal.*, 2018, **1**, 592-600.
148. M. Jouny, G. S. Hutchings and F. Jiao, *Nat. Catal.*, 2019, **2**, 1062-1070.
149. D. Wakerley, S. Lamaison, F. Ozanam, N. Menguy, D. Mercier, P. Marcus, M. Fontecave and V. Mougel, *Nat. Mater.*, 2019, **18**, 1222-1227.
150. Z. Cai, Y. Zhang, Y. Zhao, Y. Wu, W. Xu, X. Wen, Y. Zhong, Y. Zhang, W. Liu, H. Wang, Y. Kuang and X. Sun, *Nano Res.*, 2019, **12**, 345-349.
151. Y. Zhang, Z. Cai, Y. Zhao, X. Wen, W. Xu, Y. Zhong, L. Bai, W. Liu, Y. Zhang, Y. Zhang, Y. Kuang and X. Sun, *Nanoscale Horiz.*, 2019, **4**, 490-494.
152. M. Wang, L. Wan and J. Luo, *Nanoscale*, 2021, **13**, 3588-3593.
153. R. Chen, H.-Y. Su, D. Liu, R. Huang, X. Meng, X. Cui, Z.-Q. Tian, D. H. Zhang and D. Deng, *Angew. Chem. Int. Ed.*, 2020, **59**, 154-160.
154. J. Li, K. Chang, H. Zhang, M. He, W. A. Goddard, J. G. Chen, M.-J. Cheng and Q. Lu, *ACS Catal.*, 2019, **9**, 4709-4718.
155. Z.-Z. Niu, F.-Y. Gao, X.-L. Zhang, P.-P. Yang, R. Liu, L.-P. Chi, Z.-Z. Wu, S. Qin, X. Yu and M.-R. Gao, *J. Am. Chem. Soc.*, 2021, **143**, 8011-8021.
156. S. Khan, J. Hwang, Y.-S. Horn and K. K. Varanasi, *Cell Reports Physical Science*, 2021, **2**, 100318.
157. Z. Xing, L. Hu, D. S. Ripatti, X. Hu and X. Feng, *Nat. Commun.*, 2021, **12**, 136.
158. H. Yang, Y. Wu, G. Li, Q. Lin, Q. Hu, Q. Zhang, J. Liu and C. He, *J. Am. Chem. Soc.*, 2019, **141**, 12717-12723.
159. X. Chang, T. Wang, Z.-J. Zhao, P. Yang, J. Greeley, R. Mu, G. Zhang, Z. Gong, Z. Luo, J. Chen, Y. Cui, G. A. Ozin and J. Gong, *Angew. Chem. Int. Ed.*, 2018, **57**, 15415-15419.
160. H. Xu, D. Rebollar, H. He, L. Chong, Y. Liu, C. Liu, C.-J. Sun, T. Li, J. V. Muntean, R. E. Winans, D.-J. Liu and T. Xu, *Nat. Energy*, 2020, **5**, 623-632.
161. X. Wang, Z. Wang, F. P. García de Arquer, C.-T. Dinh, A. Ozden, Y. C. Li, D.-H. Nam, J. Li, Y.-S. Liu, J. Wicks, Z. Chen, M. Chi, B. Chen, Y. Wang, J. Tam, J. Y. Howe, A. Proppe, P. Todorović, F. Li, T.-T. Zhuang, C. M. Gabardo, A. R. Kirmani, C. McCallum, S.-F. Hung, Y. Lum, M. Luo, Y. Min, A. Xu, C. P. O'Brien, B. Stephen, B. Sun, A. H. Ip, L. J. Richter, S. O. Kelley, D. Sinton and E. H. Sargent, *Nat. Energy*, 2020, **5**, 478-486.
162. T.-T. Zhuang, Y. Pang, Z.-Q. Liang, Z. Wang, Y. Li, C.-S. Tan, J. Li, C. T. Dinh, P. De Luna, P.-L. Hsieh, T. Burdyny, H.-H. Li, M. Liu, Y. Wang, F. Li, A. Proppe, A. Johnston, D.-H. Nam, Z.-Y. Wu, Y.-R. Zheng, A. H. Ip, H. Tan, L.-J. Chen, S.-H. Yu, S. O. Kelley, D. Sinton and E. H. Sargent, *Nat. Catal.*, 2018, **1**, 946-951.
163. X. Wang, Z. Wang, T. T. Zhuang, C. T. Dinh, J. Li, D. H. Nam, F. Li, C. W. Huang, C. S. Tan, Z. Chen, M. Chi, C. M. Gabardo, A. Seifitokaldani, P. Todorovic, A. Proppe, Y. Pang, A. R. Kirmani, Y.

Wang, A. H. Ip, L. J. Richter, B. Scheffel, A. Xu, S. C. Lo, S. O. Kelley, D. Sinton and E. H. Sargent, *Nat. Commun.*, 2019, **10**, 5186.
164. K. Jiang, R. B. Sandberg, A. J. Akey, X. Liu, D. C. Bell, J. K. Nørskov, K. Chan and H. Wang, *Nat. Catal.*, 2018, **1**, 111-119.
165. G. Vazquez, E. Alvarez and J. M. Navaza, *J. Chem. Eng. Data*, 1995, **40**, 611-614.
166. J. Li, X. Gao, Z. Li, J.-H. Wang, L. Zhu, C. Yin, Y. Wang, X.-B. Li, Z. Liu, J. Zhang, C.-H. Tung and L.-Z. Wu, *Adv. Funct. Mater.*, 2019, **29**, 1808079.
167. T. Zhang, P. Lin, N. Wei and D. Wang, *ACS Appl. Mater. Interfaces*, 2020, **12**, 20110-20118.
168. J. Chen and L. Guo, *Appl. Phys. Lett.*, 2019, **114**, 231604.
169. G. Liu, S. K. Karuturi, H. Chen, L. Spiccia, H. H. Tan, C. Jagadish, D. Wang, A. N. Simonov and A. Tricoli, *Nano Energy*, 2018, **53**, 745-752.
170. J. Zheng, Y. Lyu, M. Qiao, R. Wang, Y. Zhou, H. Li, C. Chen, Y. Li, H. Zhou, S. P. Jiang and S. Wang, *Chem*, 2019, **5**, 617-633.
171. D. Stavenga, S. Foletti, G. Palasantzas and K. Arikawa, *Proc. R. Soc. B.*, 2006, **273**, 661-667.
172. Z. W. Han, Z. Wang, X. M. Feng, B. Li, Z. Z. Mu, J. Q. Zhang, S. C. Niu and L. Q. Ren, *Biosurf. Biotribol.*, 2016, **2**, 137-150.
173. S. M. Kang, S. Jang, J.-K. Lee, J. Yoon, D.-E. Yoo, J.-W. Lee, M. Choi and N.-G. Park, *Small*, 2016, **12**, 2443-2449.
174. A. Serrà, Y. Zhang, B. Sepúlveda, E. Gómez, J. Nogués, J. Michler and L. Philippe, *Appl. Catal. B-Environ.*, 2019, **248**, 129-146.
175. H. Zhou, T. Fan, X. Li, D. Zhang, Q. Guo and H. Ogawa, *J. Mater. Chem.*, 2009, **19**, 2695-2703.
176. X. Qian, Y. Zhao, Y. Alsaid, X. Wang, M. Hua, T. Galy, H. Gopalakrishna, Y. Yang, J. Cui, N. Liu, M. Marszewski, L. Pilon, H. Jiang and X. He, *Nat. Nanotechnol.*, 2019, **14**, 1048-1055.
177. J. Qin, K.-B. Chu, Y. Huang, X. Zhu, J. Hofkens, G. He, I. P. Parkin, F. Lai and T. Liu, *Energy Environ. Sci.*, 2021, DOI: 10.1039/D1EE00587A.
178. Y. Xu, X. Li, J. Gao, J. Wang, G. Ma, X. Wen, Y. Yang, Y. Li and M. Ding, *Science*, 2021, **371**, 610-613.
179. B. Feng, R. P. Sosa, A. K. F. Mårtensson, K. Jiang, A. Tong, K. D. Dorfman, M. Takahashi, P. Lincoln, C. J. Bustamante, F. Westerlund and B. Nordén, *Proc. Natl. Acad. Sci. U.S.A.*, 2019, **116**, 17169-17174.
180. W. Zhang, D. Wang, Z. Sun, J. Song and X. Deng, *Chem. Soc. Rev.*, 2021, DOI: 10.1039/D0CS00751J.
181. F. Geyer, C. Schönecker, H.-J. Butt and D. Vollmer, *Adv. Mater.*, 2017, **29**, 1603524.
182. J. Xu, R. Vaillant and D. Attinger, *Microfluid. Nanofluid.*, 2010, **9**, 765-772.
183. P. Dias, A. Vilanova, T. Lopes, L. Andrade and A. Mendes, *Nano Energy*, 2016, **23**, 70-79.
184. M. F. R. Samsudin, S. Sufian, N. M. Mohamed, R. Bashiri, F. Wolfe and R. M. Ramli, *Mater. Lett.*, 2018, **211**, 13-16.
185. M. Fekete, R. K. Hocking, S. L. Y. Chang, C. Italiano, A. F. Patti, F. Arena and L. Spiccia, *Energy Environ. Sci.*, 2013, **6**, 2222–2232.
186. Y. Guo, N. Zhang, X. Wang, Q. Qian, S. Zhang, Z. Li and Z. Zou, *J. Mater. Chem. A*, 2017, **5**, 7571-7577.
187. M. Fekete, W. Riedel, A. F. Patti and L. Spiccia, *Nanoscale*, 2014, **6**, 7585-7593.
188. W. J. Lee, P. S. Shinde, G. H. Go and E. Ramasamy, *Int. J. Hydrogen Energy*, 2011, **36**, 5262-5270.
189. G. Liu, W. S. Y. Wong, N. Nasiri and A. Tricoli, *Nanoscale*, 2016, **8**, 6085-6093.
190. H. J. Chen, R. H. Bo, T. P. Thanh, G. Y. Liu and A. Tricoli, *Chempluschem*, 2018, **83**, 569-576.
191. Y. K. Kho, W. Y. Teoh, A. Iwase, L. Madler, A. Kudo and R. Amarl, *ACS Appl. Mater. Interfaces*, 2011, **3**, 1997-2004.
192. G. Liu, S. K. Karuturi, A. N. Simonov, M. Fekete, H. Chen, N. Nasiri, N. H. Le, P. Reddy Narangari, M. Lysevych, T. R. Gengenbach, A. Lowe, H. H. Tan, C. Jagadish, L. Spiccia and A. Tricoli, *Adv. Energy Mater.*, 2016, **6**, 1600697.

193. R. Mueller, L. Madler and S. E. Pratsinis, *Chem. Eng. Sci.*, 2003, **58**, 1969-1976.
194. G. Y. Liu, J. Hall, N. Nasiri, T. Gengenbach, L. Spiccia, M. H. Cheah and A. Tricoli, *Chemsuschem*, 2015, **8**, 4162-4171.
195. W. S. Y. Wong, G. Liu, N. Nasiri, C. Hao, Z. Wang and A. Tricoli, *ACS Nano*, 2017, **11**, 587-596.
196. T. Q. Tran, A. Chinnappan, J. K. Y. Lee, N. H. Loc, L. T. Tran, G. Wang, V. V. Kumar, W. A. D. M. Jayathilaka, D. Ji, M. Doddamani and S. Ramakrishna, *Metals*, 2019, **9**, 756.
197. A. Lasemi, D. Xue and P. Gu, *Comput. Aided Des.*, 2010, **42**, 641-654.
198. L. Jonušauskas, S. Juodkazis and M. Malinauskas, *J. Opt.*, 2018, **20**, 053001.
199. J. Wicks, M. L. Jue, V. A. Beck, J. S. Oakdale, N. A. Dudukovic, A. L. Clemens, S. Liang, M. E. Ellis, G. Lee, S. E. Baker, E. B. Duoss and E. H. Sargent, *Adv. Mater.*, 2021, **33**, 2003855.
200. K. R. Skene, *Sustain. Sci.*, 2018, **13**, 479-492.